

X-ray Binaries in the Ultrahigh Encounter Rate Globular Cluster NGC 6388

J. Edward Maxwell¹, Phyllis M. Lugger¹, Haldan N. Cohn¹, Craig O. Heinke², Jonathan E. Grindlay³, Sonia A. Budac⁴, Gordon A. Drukier⁵, Charles D. Bailyn⁶

Received _____; accepted _____

¹Department of Astronomy, Indiana University, 727 E. Third St., Bloomington, IN 47405; tmaxwell@astro.indiana.edu, lugger@astro.indiana.edu, cohn@astro.indiana.edu

²Ingenuity New Faculty, Department of Physics, University of Alberta, Edmonton, AB T6G 2G7, Canada; heinke@ualberta.ca

³Harvard College Observatory, 60 Garden St., MS-6, Cambridge, MA 02138; josh@cfa.harvard.edu

⁴Department of Physics, University of Alberta, Edmonton, AB T6G 2G7, Canada

⁵Advanced Fuel Research, Inc., 87 Church Street, East Hartford, CT 06108

⁶Department of Astronomy, Yale University, P.O. Box 208101 New Haven, CT 06520

ABSTRACT

We report the results of a joint *Chandra-HST* study of the X-ray binary population in the massive, high-density globular cluster NGC 6388. NGC 6388 has one of the highest predicted X-ray binary production rate of any Galactic cluster. We detected a large population of 61 *Chandra* sources within the half-mass radius with $L_X > 5 \times 10^{30}$ erg s⁻¹. From the X-ray colors, luminosities, (lack of) variability, and spectral fitting, we identify five as likely quiescent low-mass X-ray binaries. Due to the extremely crowded nature of the core of NGC 6388, finding optical identifications to *Chandra* sources is challenging. We have identified four blue, optically variable counterparts to spectrally hard X-ray sources, evidence that these are bright cataclysmic variables (CVs). One showed variability of 2 magnitudes in V, indicative of a dwarf nova eruption. One other likely CV is identified by its X-ray spectrum (partial covering with high N_H) and strong variability, making five likely CVs identified in this cluster. The relatively bright optical magnitudes of these sources put them in the same class as CV1 in M15 and the brightest CVs in 47 Tuc.

Subject headings: globular clusters: individual (NGC 6388) — X-rays: binaries — novae, cataclysmic variables

1. Background

Studying the relationship between X-ray binaries (XRBs) and globular clusters continues to provide interesting clues into cluster dynamical evolution. These clusters have long been thought to be major producers of XRBs, since dense cluster cores promote the type of dynamical interactions that lead to tight binaries such as XRBs (Clark 1975; Pooley et al. 2003). These interactions include exchange interactions where a massive stellar remnant such as a heavy white dwarf or neutron star has a close encounter with an existing binary, replacing one of the other stars (Hills 1976), tidal capture by a heavy remnant of a main-sequence star (Fabian et al. 1975), or collisions of neutron stars with red giants, eventually producing ultracompact binaries with neutron stars accreting from white dwarfs (Verbunt 1987). Cataclysmic variables (CVs) and low-mass X-ray binary (LMXB) systems are common products of these interactions (Ivanova et al. 2006, 2008). In globular clusters, a significant number of millisecond pulsars (MSPs) have been identified, such as in 47 Tuc (Camilo et al. 2000). Such systems are the likely progeny of LXMBs (Archibald et al. 2009). Since mass segregation causes the more massive populations of binary stars and degenerate remnants (for instance, MSPs) to be more centrally concentrated, these objects will be strongly tied to the dynamical evolution of the cluster. Most significantly, this increases the likelihood of further interactions of binaries in the core which can then halt the progress of dynamical relaxation, supporting the core against core collapse (Fregeau 2008).

The known distances, reddenings, and ages of globular clusters allow for an analysis of populations of CVs and LMXBs that is not possible for field objects. Using the Hubble Space Telescope (*HST*) in conjunction with the Chandra X-ray Observatory (*Chandra*) large numbers of X-ray sources have been identified in clusters and matched to optical counterparts. For instance, Heinke et al. (2005) detected 300 X-ray sources down to $L_X \sim 8 \times 10^{29} \text{ erg s}^{-1}$ within the half-mass radius of 47 Tuc, 105 of which could be

securely classified as quiescent LMXBs (qLMXBs), CVs, MSPs, or chromospherically active binaries (ABs), mostly by using HST to identify and characterize optical counterparts (Edmonds et al. 2003a,b). Similar identifications were also made of 59 of the 79 X-ray sources detected (with limiting $L_X \sim 10^{29}$ erg s $^{-1}$) in NGC 6397, a cluster that has undergone core-collapse, by Cohn et al. (2010) in a joint *HST-Chandra* study.

Higher numbers of interactions in cluster cores lead to larger populations of X-ray sources (Pooley et al. 2003). This interaction rate can be simply estimated by the encounter rate, $\Gamma \propto \rho_0^2 r_c^3 / v_0$ (Verbunt & Hut 1987; Maccarone & Peacock 2011). This quantity is a measure of how often stellar interactions will occur as a function of the cluster’s central density, core radius and central velocity dispersion. The numbers of X-ray sources in a cluster, particularly the qLMXBs, MSPs, and brighter CVs, vary directly with this encounter rate, implying strongly that dynamical interactions are the primary source of these populations in globular clusters (Pooley et al. 2003; Heinke et al. 2003; Pooley & Hut 2006), while fainter ABs seem to be largely primordial in origin (Bassa et al. 2004).

1.1. NGC 6388

NGC 6388 is a particularly good candidate for the study of the dynamical origin of XRBs in dense-core globular clusters due to its large central density ($10^{5.34} L_\odot \text{pc}^{-3}$) and core radius ($7.2'' = 0.35$ pc at 9.9 pc from the Sun) (Harris 1996)¹. These give it one of the largest values of Γ of any globular cluster in the Galaxy. With such a large encounter rate, we expect it to host a rich population of LMXBs and CVs, and thus to find a large number of X-ray sources. In Lugger et al. (1987), the U-band surface brightness profile, which is dominated by horizontal branch stars, was found to be well fit by a single mass King model,

¹<http://physwww.physics.mcmaster.ca/~harris/mwgc.dat> for 2010 revision.

suggesting that the core is likely being supported by a large number of primordial binaries. It is possible that some of these primordial binaries could be detected now as ABs.

NGC 6388 also has several features beyond its large encounter rate that make it a cluster worth investigating. For instance, for a cluster of its metallicity (as high as $[\text{Fe}/\text{H}] \approx -0.7$ (Wallerstein et al. 2007), it has a rather atypical extreme blue horizontal branch (EBHB) in addition to a blue horizontal branch (BHB), and a very populated red horizontal branch (RHB). Rich et al. (1997) investigated whether this could be the result of dynamical interactions in the core enhancing the BHB via stripping of the envelope mass. However they found no difference in the radial distribution of the RHB and BHB stars and took this as evidence against the dynamical argument. Also intriguing are the blue hook stars (hotter and less luminous than EBHB stars), investigated in Dalessandro et al. (2008). Noyola & Gebhardt (2006) report evidence for a modest central cusp in the surface brightness profile and Lanzoni et al. (2007) see a modest central surface density cusp in the inner arcsec, which are interpreted by those groups to be evidence for a central intermediate-mass black hole (IMBH) of mass $5.7 \times 10^3 M_\odot$. Cseh et al. (2010) show that their radio nondetection gives an upper limit to the mass of a central IMBH that is less than half the mass predicted by Lanzoni et al. (2007). Recently Lützgendorf et al. (2011) used stellar kinematics to argue for a central IMBH with a mass of $17 \pm 9 \times 10^3 M_\odot$. Miocchi (2007) suggests that tidal stripping of red giant envelopes by this putative IMBH may be producing the significant population of EBHB stars.

Verbunt (2001) analyzed two ROSAT PSPC observations of NGC 6388 from 1991 and 1992, identifying an X-ray source at $L_X(0.5\text{-}2.5 \text{ keV})=6 \times 10^{33}$ ergs/s just outside the half-mass radius. We do not detect a source in the smaller of Verbunt’s two error circles. This could indicate a transient was active during the ROSAT observations, and faint in quiescence during the *Chandra* observations. It also could indicate that Verbunt’s ROSAT

astrometry was incorrect, since the luminosity is close to our measured total L_X for the cluster. Less sophisticated X-ray analyses of our Chandra observation and a 2003 XMM observation, with the goal of constraining the presence of an intermediate-mass black hole at the cluster center, were performed by Cseh et al. (2010); Nucita et al. (2008).

Evidence that NGC 6388 contains at least one transient X-ray binary (in agreement with predictions of its high stellar encounter rate) was provided by IGR J17361-4441, a hard X-ray transient located in NGC 6388. It was detected by INTEGRAL on August 11, 2011, with follow up observations by Swift, RXTE, XMM, ATCA, and *Chandra*. It had a peak output in the 0.5-10 keV energy band of $L_X \sim 5 \times 10^{35}$ ergs/s (Bozzo et al. 2011; Nucita et al. 2012). A short *Chandra* target of opportunity observation provided a precise position, inconsistent with any of the cluster X-ray sources we present below, allowing an upper limit on the transient’s quiescent luminosity of 10^{31} ergs/s (Pooley et al. 2011). In the last Swift observation of Nov. 4, 2011 (before solar proximity forbade observations), this transient was still active at similar luminosities, but the X-ray emission from the cluster was consistent with the normal quiescent output by Jan. 29, 2012 (Bozzo et al. 2012).

2. Data

2.1. *Chandra* Observations

We obtained a 45 ks ACIS-S² observation of NGC 6388 on 2005 April 21/22, with the center of the cluster placed on the S3 chip. We chose the S3 chip for its high sensitivity and spectral resolution. We used the timed exposure mode with the very faint telemetry format. The moderate reddening of NGC 6388 ($E(B - V) = 0.37$, Harris 1996 (2010 version)) gives a moderate hydrogen column density, $N_H \sim 2.2 \times 10^{21}$ cm⁻². A detection limit of 2 counts,

²Advanced CCD Imaging Spectrometer/S-Array

for the 45 ks ACIS-S exposure, corresponds to a flux of $f_X \approx 4 \times 10^{-16}$ erg s $^{-1}$ cm $^{-2}$ in the 0.5–6.0 keV energy band for a power-law spectrum with a photon index of 2. Assuming a distance of 9.9 kpc (Harris 1996 (2010 version)), this limiting flux corresponds to a luminosity of $L_X \approx 5 \times 10^{30}$ erg s $^{-1}$. We are complete to ~ 5 counts, except in the core and near bright sources. We are likely complete to ~ 10 counts except very near to bright sources. In Fig. 1 we plot the location of the identified X-ray sources on the X-ray image. We constructed a false-color representation of the sources, Fig. 2, where the variety of soft and hard X-ray sources is easily noted.

2.2. *HST* Observations

Our optical analysis is based on ACS/HRC³ imaging obtained in 2003 and 2006 through the F555W (hereafter V_{555}) and F814W (hereafter I_{814}) filters (GO-9835 and GO-10474, PI: Drukier) and imaging obtained in 2006 through the F330W (hereafter U_{330}) filter (GO-10350, PI: Cohn). We refer to the filters used in a way that suggests similarity to the Johnson system, but with subscripts to indicate that the obtained data is not transformed to that system, especially true in the F330W filter, which is both bluer and narrower than the Johnson U filter. Table 1 lists the data sets, dates, filters, and exposure times. The observations used heavy dithering, with integer pixel plus subpixel offset, in order to allow for bad pixels and to increase the effective resolution through drizzle reconstruction of the frame. Rather than using the standard STSDAS *multidrizzle* algorithm, we used images created through a similar procedure, applied by J. Anderson. The resulting drizzle-reconstructed U_{330} image is shown in Fig. 3. We note that while the dithering substantially improves the effective resolution by about a factor of two, the core

³Advanced Camera for Surveys/High Resolution Channel

region of NGC 6388 remains very crowded, with a considerable amount of psf overlap.

3. X-ray Analysis and Results

We reprocessed the *Chandra* data using CIAO 3.2, CALDB v.3.0.2, and standard procedures⁴. This involves identifying and excluding bad pixels, utilizing information kept in the VFaint telemetry format to reduce background, using accurate time-dependent gain and CTI corrections, removing pixel randomization, and selecting for grade and status. No background flares were seen, so we used the full 45.16 ks of live observing time.

3.1. X-ray source identification

We used the CIAO *wavdetect* program on *Chandra* images of the cluster within the half-mass radius, in the 0.3-6 and 0.3-1.2 keV energy ranges, to detect 61 sources. The source positions were refined, and net counts and spectra extracted, using the IDL package *acis_extract* (Broos et al. 2010); see Table 3. Using the net counts, and a conversion from counts to flux for each of 7 narrow bands, we computed an X-ray color-luminosity diagram (Fig. 4). Five sources (marked as squares) have relatively soft X-ray colors while being relatively luminous ($L_X > 10^{32}$ erg s⁻¹). We plot the expected positions in this diagram of a 10-km radius, 1.4 M_\odot neutron star (NS) with low B-field and a hydrogen atmosphere (NSATMOS, Heinke et al. 2006). The five soft sources are consistent with this line, or slightly harder (which may indicate a spectrum containing both a NS atmosphere and a harder component). By comparison with similar diagrams in other globular clusters (Heinke et al. 2003; Pooley & Hut 2006), we infer that the harder sources (consistent with

⁴<http://cxc.harvard.edu/ciao/threads/all.html>

e.g. a power-law of photon index 1.5) are predominantly CVs. Below we identify evidence for the CV nature of five of them (labeled with blue triangles).

3.2. X-ray Spectral Analysis

Below we discuss X-ray spectral analysis of those sources with more than 80 counts. Our principal objective was to identify which sources have spectra typical of quiescent LMXBs, vs. which sources have spectra more commonly associated with cataclysmic variables. We used spectral fits of a power-law, MEKAL (hot thermal plasma, with the cluster abundance of -0.6, or 25%; Liedahl et al. 1995) which is often appropriate for fitting CVs, and NSATMOS + power-law (typical of quiescent LMXBs, Heinke et al. 2006). We performed spectral fits in which we binned all spectra, using 20 counts/bin for brighter sources and 10 cts/bin for sources below 150 counts, and directly on the unbinned data using the C statistic. The results from these fits were similar, but the unbinned spectral fitting allowed better constraints, particularly on the fraction of flux in the (above ~ 2 keV) power-law component in NS+power-law spectral fits. Results from the unbinned spectral fits are presented in Table 4, while example binned spectral fits are presented in Fig. 5. For all fits we imposed a minimum N_H of 2.2×10^{21} cm $^{-2}$, the value inferred from the reddening.

3.2.1. Strong candidates for quiescent LMXBs

Five sources (CX1, CX2, CX3, CX8, and CX10; Table 4) require very large photon indices (> 3) when fit by a power-law model, or very low MEKAL temperatures (< 1.5 keV) for that model. Spectral fits to NSATMOS models plus power-law components give excellent fits without need of the power-law component, which can be constrained to $< 30\%$ of the 0.5-10 keV flux (for assumed photon index of 1.5, e.g. Cackett et al. 2010). In four

of them, the power-law component can be constrained to $< 13\%$ of the flux. We take these spectral fits as strong evidence for a quiescent LMXB interpretation. Combined with the location of all five within or close to the cluster’s core, and the lack of bright optical counterparts (which argue against foreground coronal sources), we conclude that these five are quiescent LMXBs.

3.2.2. Hard X-ray sources

Most of the remaining brighter X-ray sources have spectra consistent with typical CVs in other clusters—consistent with high-temperature ($\sim 5\text{--}10$ keV) MEKAL models with absorption similar to the cluster value (Table 4). However, CX4 has a very hard spectrum (photon index $\Gamma = 0.9^{+0.4}_{-0.4}$). This suggests a CV nature, as CVs tend to have hard intrinsic spectra, and have more intrinsic absorption than active binaries or millisecond pulsars. This source cannot be well fit by MEKAL models using standard absorption (see Table 4, Figure 5). It can be well fit by a simple absorbed power law, but with a photon index of $0.30^{+0.45}_{-0.39}$, unusually flat for an intrinsic X-ray spectrum. A partial covering absorber model, commonly used for intermediate polar CVs, provides a good (59% “goodness”) fit; using N_H (PHABS) of 2.2×10^{21} plus a PCFABS component covering 92% of the emission with 3.9×10^{22} cm $^{-2}$. This gives $kT = 3.7^{+2.2}_{-1.5}$ keV, and $L_X = 2^{+1.2}_{-0.7} \times 10^{33}$ erg s $^{-1}$. The high luminosity and hard spectrum suggestive of partial covering suggest that this source may be an intermediate polar CV.

3.3. X-ray source variability

We used the *glvary* program in CIAO (Gregory & Loredo 1992) to search for variability in all X-ray sources with more than 30 counts. Only one source produced a significant

detection of variability, CX4, which produced an odds ratio of $10^{14.4}$ and probability of 1.0 of variability. Its lightcurve (along with that of a typical nonvariable source, CX2, with odds ratio $10^{-1.3}$ and probability 0.043) is shown in Fig. 6. We note that the quiescent LMXBs in NGC 6388 do not show obvious variability, as expected if their X-ray emission arises from reradiation of heat stored in the deep crust (Brown et al. 1998; Ushomirsky & Rutledge 2001). Some quiescent LMXBs have shown clear variability in their thermal emission (Fridriksson et al. 2010; Cackett et al. 2010), but the subset of quiescent LMXBs without a strong power-law spectral component have not yet shown evidence for such variation (Heinke et al. 2006).

3.4. X-ray Source Distribution

By examining the spatial distribution of the X-ray sources in NGC 6388, we may infer the masses of the objects from which the X-ray fluxes originate (see for instance the discussion in Cohn et al. 2010). We compare the distribution of the X-ray sources to the cluster parameters derived from the distribution of stars used in finding the center of the cluster (see §4.3). We expect the X-ray sources to be more centrally concentrated, and thus more massive, assuming the populations are in thermal equilibrium. As with previous studies (Grindlay et al. 2002; Cohn et al. 2010) we fit the different populations with generalized King models:

$$S(r) = S_0 \left[1 + \left(\frac{r}{r_0} \right)^2 \right]^{\alpha/2}, \quad (1)$$

where r_0 is related to the core radius r_c by

$$r_c = (2^{-2/\alpha} - 1)^{1/2} r_0. \quad (2)$$

Using the stars with $V_{555} < 20.0$, we find the optical distribution of NGC 6388 to be well fit by $r_c = 7.2$ arcsec and $\alpha = -2$. If we assume thermal equilibrium, the slope parameter for the X-ray sources α_X is related to the slope parameter for the optical distribution α_0 by

$$\alpha_X = 1 + q(\alpha_0 - 1) \quad (3)$$

where $q = M_X/M_*$ is the ratio of the characteristic mass of the X-ray sources to the mass of the objects that dominate the optical light distribution. We fit the King model using a maximum-likelihood algorithm. We then applied a bootstrap method, where 1000 resampled populations are created by resampling from the original population until the total number is reached, replacing the chosen source back into the pool before each choice. We used the set of these resampled populations to determine uncertainties of the best-fit parameter values by fitting the King model to each resampled population and then analyzing the resulting distribution of the best-fit parameter values. The uncertainty in each parameter was set equal to half of the 68% spread of the best-fit parameter values about the median. For the fits we used the center of the cluster as determined from the optical data (see §4.3).

Since the cluster lies in a region where the Galactic ridge emission is weak ($l=345.56^\circ$ and $b=-6.74^\circ$, Harris 1996 (2010 edition); see the map in Revnivtsev et al. 2006), the background contamination was only determined using Eqn. 1 in (Giacconi et al. 2001) to estimate extragalactic contamination. We find that over the area covered by all the detected sources, there are likely 2-3 background source detections. In an effort to verify this value, we performed an additional fit including the additional parameter B_0 for the background to Eqn. 3.4, as in Elsner et al. (2008). This gave a result for B_0 that was consistent with our previously calculated value.

The fit for the distribution of the X-ray sources by a King model profile along with a term for background sources is seen in Fig. 7. It is plotted alongside the distribution for the stars with $V_{555} < 20.0$ for comparison. From the fits (see Table 6), we find the ratio of X-ray source mass, M_X , to the typical mass of stars with $V_{555} < 20.0$ to be $q = 1.51 \pm 0.12$.

We can infer the mass of the stars used to determine the cluster parameters by comparison with 47 Tuc, which Catelan et al. (2006) have found to be very similar in composition and age to NGC 6388. Heinke et al. (2005) found that for the range of stars in 47 Tuc similar to those we used to determine the optical profile for NGC 6388, the average mass was approximately $0.88 \pm 0.05 M_\odot$. We use the approximate value of $0.9 M_\odot$, to infer a mean X-ray source mass of $1.36 \pm 0.11 M_\odot$. This is consistent with a mixture of massive cataclysmic variables and low mass X-ray binaries. For comparison, Cohn et al. (2010) reported a mass of $1.14 \pm 0.14 M_\odot$ for CVs in NGC 6397. And for 47 Tuc, Heinke et al. (2005) found a mass of $1.43 \pm 0.17 M_\odot$ for all of the detected X-ray sources, and $1.31 \pm 0.22 M_\odot$ for the identified CVs.

We also fit the identified qLMXBs, but ignored background contamination due to the small sample. This gave a value of $q = 1.63 \pm 0.31$, which corresponds to a mass of approximately $1.47 \pm 0.28 M_\odot$. While the difference in mass is not statistically significant, it is suggestive that the qLMXBs are more massive than the other X-ray sources (see Fig. 8). We also can compare the bright X-ray sources, defined as those with counts > 40 , with the faint X-ray sources. The fits to these two populations can be found in Table 6 and their distributions are plotted in Fig. 9.

We use a Kolmogorov-Smirnov (K-S) test on two samples to determine the likelihood of their radial distribution being drawn from the same population of stars. We find they are consistent with being from the same distribution at a probability of only 9%. While this does not represent a high level of statistical significance, it suggests that bright X-ray

sources may be more centrally concentrated than fainter ones, similar to that seen in NGC 6397 for the bright CVs (Cohn et al. 2010). This may indicate that dynamical interactions scatter hard binaries into elongated orbits where they dim as they age.

4. *HST* Data Analysis and Results

4.1. Astrometry

We put the ACS/HRC frames on the ICRS astrometric grid by first obtaining an astrometric solution for a ground-based frame, then using this frame to define secondary astrometric standards, and finally using these secondary standards to obtain a solution for the ACS frames. The ground-based frame, from the ESO archive, was taken with the Superb Seeing Imager 2 (SUSI2) on the ESO New Technology Telescope (NTT) on 2003 May 05 with a field of view of $5.46' \times 5.75'$. The primary astrometric standards are from the second US Naval Observatory CCD Astrograph Catalog (UCAC2), which has an RMS uncertainty of 70 mas (Zacharias et al. 2004). Consistent with this uncertainty, the astrometric solution for the ESO frame using 108 primary standards had an RMS uncertainty of 72 mas. Since the internal error of the ACS astrometric solution using 15 secondary standards is about 13 mas, the overall accuracy of the astrometric solution of the ACS images is 73 mas. We took the corrected *HST* coordinates to be our fundamental coordinate system and applied a boresight correction to the *Chandra* source positions as described below in section 4.4.

4.2. The Color-Magnitude Diagram

We used DAOPHOT-ALLSTAR to carry out PSF-fitting photometry on the two stacked V_{555} frames (2003 and 2006 epochs) and on the single stacked U_{330} frame (2006 epoch). The

PSF was constructed using about 100 stars with the least crowding in the frames, with an iterative approach to neighbor subtraction. We constructed the PSF by first solving for it with a total radius that was relatively small: about twice the FWHM of the stars in the image. After each solution for the psf, a subtracted frame was constructed to clean the region around the chosen psf stars. A new psf with a larger radius was determined from this cleaner frame. This process was iterated until the change in the error to the psf fit became negligible. A total of 28612 objects were jointly detected in the 2006 V_{555} and U_{330} data.

The magnitudes were calibrated to the STMAG system using the method described by Sirianni et al. (2005). Since the stacked images used for our PSF analysis had an arbitrary normalization, we constructed a second set of stacked images using *multidrizzle*. We then obtained aperture photometry from a subset of our stars from these images to the STMAG system. Specifically, we used the psf stars we had chosen for the DAOPHOT-ALLSTAR analysis. These magnitudes were converted to the STMAG system and then an offset was found between these derived magnitudes and the previously measured psf photometry. This offset was then applied to all the psf magnitudes in each of the filters and epochs.

Figure 10 shows the resulting ($V_{555}, U_{330} - V_{555}$) CMD for the 2006 epoch – the epoch for which both U and V band imaging are available. The previously noted features of the CMD, discussed in §1.1, are apparent: the sloped red horizontal branch, the BHB, and the EBHB. Also we see a large blue straggler (BS) population, although the smearing out of the fiducial sequences makes it difficult to select blue stragglers near the main sequence turn-off (MSTO) with certainty. The MSTO lies about 3.7 magnitudes below the mean magnitude of the RHB and the MS extends about another 1.5 mag below the MSTO. Of note is the extension of the EBHB to about 1 mag below the MSTO and the presence of stars that lie below the MSTO and which are much bluer than the MS. As we discuss in §4.5 below, some of these stars appear to be counterparts to *Chandra* sources. It is useful to compare these

results to those of Catelan et al. (2006), who have presented a deep *HST*-based CMD of NGC 6388. They used data from the *HST* SNAP-9821 and GO-9835 datasets; the former was obtained with the ACS/WFC while the latter, which was obtained with ACS/HRC for the present program, provides higher angular resolution. Their analysis of these data with DAOPHOT-ALLFRAME produced a $(V, B-I)$ CMD. While their overall CMD is relatively similar to ours, taking into account the different color indices used, we note that the EBHB in our CMD extends to an additional 2.5 magnitudes below the RHB, i.e. a total of 4.4 mag below the RHB. While the tip of the EBHB region is relatively sparsely populated, it raises many questions regarding stellar evolution (see, for instance, the discussion by Brown et al. 2010).

4.3. Optical Radial Distribution

The high resolution of the cluster core provides an opportunity to measure the position of the cluster center and analyze the radial distributions of the different populations of stars seen in the optical. To avoid problems with completeness, we use only stars brighter than 20 in V_{555} to determine the optical center of the cluster in the ICRS reference frame. This sample is used specifically to mirror the evaluation of the cluster center as described in Lanzoni et al. (2007). The centering method involved iterative centroiding over a circular aperture of radius $9''$. Using this sample of stars we find a center of $RA = 17^h 36^m 17.185^s \pm 0.12''$ $dec = -44^\circ 44' 06.44'' \pm 0.12''$. To find errors for the center, we use the bootstrap method as described in §3.4. We find that due to the small field of view for the ACS/HRC, the center cannot be determined to better than about 0.12 arcsec. This is because the cluster’s core fills much of the field of view, giving little leverage for determining the center.

In Fig. 11, we compare our computed center with other recently reported cluster centers. We find that our center differs by about 2–3 σ from the centers determined by

Lanzoni et al. (2007) and Lützgendorf et al. (2011), lying somewhat to the north west. With our higher resolution, we were able to count more stars than either study, which may account for the differences. Note that the center derived by Noyola & Gebhardt (2006) was from a frame that was not corrected to a standard world coordinate system, which (as they point out) can be significant in *HST* fields.

The stars used for finding the cluster center were then used to solve for the cluster parameters using maximum-likelihood routines to fit a generalized King model to the distribution (see Eqns. 1 and 2). Bootstrap statistics are used to determine errors on the fit. These stars give a value of 7.1 ± 0.2 arcsec for the core radius and -2.04 ± 0.08 for the slope of the fall off. These are consistent with previous solutions of 7.2 arcsec and -2.0, respectively (Harris 1996), which we use for comparison with other populations of interest.

We fit several different stellar sub-populations in the same way as we fit the X-ray distributions (Table 6). We see that the RHB core radius fit is consistent with the parameters previously found for this cluster of 7.2 arcsec. We also find it has an $\alpha = -1.92 \pm 0.33$, which is consistent with the parameters for a relaxed system. A K-S test shows that the RHB distribution is consistent with the distribution of the other stars with $V_{555} < 20.0$ (Table 5). Since HB stars will typically be less massive than the RGB stars that make up a majority of the stars with $V_{555} < 20.0$, we assume they have not yet re-thermalized at their new masses.

Fitting the blue stragglers (BSs) in the cluster shows them to be significantly more centrally concentrated than the stars with $V_{555} < 20.0$. We infer a mass of 1.80 ± 0.27 times the mass of the stars with $V_{555} < 20.0$, giving a mass of approximately $1.62 M_{\odot}$ for the BSs. When we plot these distributions, we can see how the BSs stand out from the stars with $V_{555} < 20.0$, while the RHB is consistent with that population (Fig. 12). When we compare the BSs to the stars $V_{555} < 20.0$ with a K-S test, we find they are not the same, with a

probability of less than 1% of being drawn from the same underlying population (see Table 5). This is in agreement with the significant difference in the masses we find for the two populations.

We also compare the distributions of the RHB, BHB, and EBHB stars to see if any one is more centrally concentrated than the others as a test for the influence of dynamical effects on the differences between these populations. K-S tests show that there is no significant difference in the radial distributions of the RHB, BHB, and EBHB. Thus we find no difference in the masses of these three groups of stars. This result is in agreement with previous findings for these populations (Rich et al. 1997; Dalessandro et al. 2008).

4.4. Boresight Correction

From the CMD, a very blue star was easily picked out. This star coincides with one of the brighter X-ray sources (source CX5), and provided a preliminary boresight correction to the X-ray positions. After applying this correction, we attempted to discover additional counterparts from their position in the color-magnitude diagram and proximity to X-ray source positions. But of the stars for which U_{330} and V_{555} magnitudes were obtained through the standard procedures, there were none that could be identified in this way. Fortunately, three additional optical counterparts were identified by blinking the images in two bands (U_{330} from 2006 against V_{555} from 2003 and 2006) and searching for blue stars near the X-ray positions. Using these four counterparts, a final correction of 0.105 arcsec in RA and -0.031 arcsec in Dec was applied to the *Chandra* positions, well short of the 90% pointing error circle of ~ 0.6 arcsec. Once this correction was applied, we searched for additional counterparts. In the region near source CX11, a blue object was identified visually. Unfortunately it lies in the Airy ring of a much brighter star, preventing accurate photometry. We also extended our search to objects with a red excess in the U_{330} , V_{555} , and

I_{840} bands in search of millisecond pulsars and active binaries. These additional searches yielded no other detectable optical counterparts.

The small number of detected counterparts is not surprising considering that the factors that predict a large number of X-ray sources in NGC 6388 also make doing deep photometry challenging. Since the likely counterparts to X-ray sources are most likely to be centrally concentrated, the optical images were centered on the cluster. Because of the small field of view of the HRC on the ACS, the moderately large core radius represents a significant fraction of the entire field. As the core is also very dense, most of the optical counterparts must be found against a bright background of the core stars, making sky subtraction unreliable for objects more than about 3 mag below the MSTO. This also results in X-ray sources somewhat outside the core (such as CX4) falling outside of the field of view in the optical images.

4.5. Analysis of Optical Counterparts

We performed photometry for each of the identified optical counterparts using DAOPHOT-ALLSTAR on combined, drizzled frames for each of the epochs (Table 2). One can see from the CMD (Fig. 10) that these four stars lie well to the blue of the main sequence (MS) and near the limit of detection in the V_{555} frames. For three of these stars, a light curve was constructed using aperture photometry performed on the original, undrizzled frames. The points were then further binned to provide a statistical data set with which we could test the variability of the optical sources. For the dimmest counterpart in the densest part of the field (source CX7), measuring in undrizzled frames was not possible in either the 2003 or 2006 epoch. In this case, we drizzled and combined the data into three images. For reference, finding charts are shown in Fig. 13.

4.5.1. Source CX5

CX5’s counterpart is extremely blue ($U_{330} - V_{555} = -1.2$). The Airy disk from a brighter nearby star makes I_{814} measurements impossible. Our V_{555} light curves for 2003 and 2006 (Fig. 14) show variability of 0.6 and 0.8 mags (respectively), on timescales of hours. The 2003 variability suggests sinusoidal variations with $P > 8$ h, but the amplitude is extremely high for ellipsoidal variability (typically 0.1 mags, e.g. Edmonds et al. 2003b). The companion’s average brightness drops by 0.7 mags from 2003 to 2006. The size of these changes may suggest dwarf nova eruptions, which are typically 2-5 mags (e.g. Shara et al. 1996), although disk flickering cannot be excluded. Using the distance of 9.9 kpc from Harris (1996, 2010 version) and correcting for extinction, the source has a bright absolute magnitude of 6.99. The absolute magnitude $M_{V_{555}}$ and L_X of CX5 place it among the more luminous X-ray CVs known in clusters.

4.5.2. Source CX7

We discovered the possible counterpart for source CX7 (as well as the counterparts for sources CX9 and CX12) by blinking the drizzled U and V images and looking for obvious blue sources near the error circles of the X-ray sources. CX7’s optical counterpart is clearly blue ($U_{330} - V_{555} = -0.58$), although accurate photometry is difficult due to its being located in one of the densest parts of the cluster. In order to construct a light curve for this nearly blended source, we drizzled the image sets from 2003 into three images, which clearly require hours-timescale variability (change of 0.5 mags) (The star in the 2006 epoch was too low in signal in all the images for this procedure to work.) Plotting these data and their associated errors shows the star’s luminosity is not consistent with a constant source (see Fig. 14). The absolute magnitude of the counterpart in 2006 is $M_{V_{555}} = 6.89$. In view of this object’s optical variability and location in the CMD, and the X-ray source properties

(§3.2.2), we conclude the optical object is a bright CV and the optical counterpart to source CX7.

4.5.3. Source CX9

The optical counterpart for this source is very blue ($U_{330} - V_{555} = -0.60$). It appears very bright ($M_{V_{555}}=3.79$) in the 2003 V data, but is much dimmer ($M_{V_{555}}=6.065$) in 2006. It shows variability in the V_{555} of 0.2mag over the observation in 2003, and 0.6 mag in 2006 (Fig. 14). From the curve for 2003, we find a lower limit for the period of variation of about 8h. Of our counterparts, this is the most convincing case for ellipsoidal variation with its small magnitude change, indicating a possible 20-h period. Dramatically, between the 2003 epoch and the 2006 epoch, the optical object shows a difference in magnitude of more than 2 mags. This is consistent with dwarf nova eruptions observed in globular clusters (e.g. Shara et al. 1996, 2005). As this object also has similar optical properties to the counterpart for source CX5, we use the same argument to identify it as a CV.

4.5.4. Source CX12

This counterpart to CX12 is very blue ($U_{330} - V_{555}=-0.49$). The counterpart is very bright with $M_{V_{555}}=6.68$ in 2006. Over the 2003 observations it shows variations of 0.2 mag and in the 2006 epoch it varies by ~ 0.5 mag (Fig. 14). In light of CX12’s CV-like X-ray properties, the nature of its optical variation, and its position in the CMD, we conclude that it is consistent with a bright CV.

5. Discussion

We find a rich population of X-ray sources in NGC 6388. Our analysis of the density profile for the X-ray sources shows them to be more centrally concentrated than the brightest stars in the cluster. The inferred characteristic mass of $1.36 M_{\odot}$ for the X-ray sources suggests that many of them are likely to be compact binary stars with degenerate remnant primaries. Many of these were likely produced in close interactions in the cluster’s large, dense core.

We examine some of the characteristics of the different populations of the optical sources. The extensive population of blue stragglers was shown to be more massive than the horizontal branch stars. The distinctive extreme blue horizontal branch stars were shown to be no different in distribution than the other horizontal branch stars, confirming the result that dynamical interactions are not a likely cause of the large color distribution in the cluster’s horizontal branch.

We identify five sources as bright CVs based on their X-ray luminosities and colors, together with the detection of optical counterparts for four of them, and the detection of X-ray variability for the remaining one. These counterparts are consistent with bright CVs in optical variation, color, and luminosity. In fact, we find at least one of the sources (CX9) to exhibit variation on par with that exhibited by dwarf nova outbursts. That would make it only the 15th such object found in globular clusters to date (see Servillat et al. 2011). The only CV candidate without an identified optical counterpart, CX4, was identified as a likely CV based on its X-ray properties; an unusually hard spectrum, well-fit by partial covering absorption models, luminosity, and variability. We find five sources that have X-ray colors, luminosities, and spectra consistent with what we expect for qLMXBS. These sources are not found to vary, which is consistent with expectation for sources without a strong power-law component.

The CVs found here are some of the brightest (in X-rays and optical light) yet known in globular clusters, suggesting relatively high mass transfer rates. These are likely the tip of a much larger CV population. The limit of our detection of CVs was $V_{555} < 23.1$, for which we detected 4 bright CVs as optical counterparts to X-ray sources. We can extrapolate the possible size of the CV population in NGC 6388 by comparison with other clusters with bright CVs and a detected CV population. 47 Tuc was found to have at least 22 CVs by Edmonds et al. (2003a) looking to 8 magnitudes fainter than the MSTO. After adjusting for distance and reddening, there are 4 CVs in 47 Tuc with magnitudes similar to those in NGC 6388. We can infer that the population of CVs in NGC 6388 is likely as large as that of 47 Tuc. This is not surprising given the similarities between the two clusters and that they both have some of the highest encounter rates of any cluster (see below).

The large number of sources detected in our data is consistent with predictions based on the encounter rate. We can estimate the encounter rate using the approximation given in Verbunt (2003), $\Gamma \propto \rho_0^2 r_c^3 / v_0$. We use values from Harris (1996) (2010 edition) for ρ_0 , r_c , and v_0 for this approximation. In Table 7, we give our calculation for this value for the clusters studied in Pooley et al. (2003) and for NGC 6388 and compare these to the number of detected X-ray sources with $L_X > 4 \times 10^{30}$ erg s⁻¹ in the 0.5-6 keV range. We have normalized our values of Γ to the mean of the values given for the non-core collapsed clusters in Pooley et al. (2003). We find them to be roughly consistent, with major differences likely due to our use of the updated Harris catalog. NGC 6388's approximate Γ is seen to be significantly larger than that of all but one of the other clusters. In the table we also compare the number of detected sources reported by Pooley et al. (2003) with the number detected in more recent studies (as noted in the table comments). The larger numbers detected in more recent studies may be attributed to improved reduction techniques that allow for a better separation of sources in crowded regions. Ultimately, the only two clusters to show a significant difference are ω Cen and 47 Tuc, which are most

affected by the changes in their values for Γ , a result of using updated values for the cluster parameters.

In Fig. 15, we plot the number of detected sources, using the newest values when possible and correcting for the predicted background contamination, versus Γ . We note that detections for NGC 6388 and NGC 6093 (M80) are not complete to $L_X > 4 \times 10^{30}$ erg s⁻¹ (see §2.1), so their detected source numbers are lower limits (indicated with arrows). We fit the relationship of Γ and N with a power law and find it can be described as $N \propto \Gamma^{0.55 \pm 0.09}$. This corresponds with the result of Pooley et al. (2003), where a similar trend was found with their calculated values of Γ . In light of this trend, the detection of X-ray sources in NGC 6388 is a confirmation of the prediction that its large, dense core produces a large number of close stellar interactions, which in turn accelerate the production of close binary systems.

This research is supported by NASA grants GO5-6045X and HST-GO-10350.01-A to Indiana University. COH and SAB thank NSERC, and COH thanks the Alberta Ingenuity New Faculty program, for funding.

REFERENCES

- Archibald, A. M., et al. 2009, *Science*, 324, 1411
- Bassa, C., Pooley, D., & Homer, L. e. a. 2004, *ApJ*, 609, 755
- Bassa, C. G., Pooley, D., Verbunt, F., Homer, L., Anderson, S. F., & Lewin, W. H. G. 2008, *A&A*, 488, 921
- Bogdanov, S., van den Berg, M., Heinke, C. O., Cohn, H. N., Lugger, P. M., & Grindlay, J. E. 2010, *ApJ*, 709, 241
- Bozzo, E., et al. 2011, *A&A*, 535, L1
- . 2012, *The Astronomer’s Telegram*, 3958, 1
- Brown, E. F., Bildsten, L., & Rutledge, R. E. 1998, *ApJ*, 504, L95+
- Brown, T. M., Sweigart, A. V., Lanz, T., Smith, E., Landsman, W. B., & Hubeny, I. 2010, *ApJ*, 718, 1332
- Cackett, E. M., Brown, E. F., Miller, J. M., & Wijnands, R. 2010, *ArXiv e-prints*
- Camilo, F., Lorimer, D. R., Freire, P., Lyne, A. G., & Manchester, R. N. 2000, *ApJ*, 535, 975
- Catelan, M., Stetson, P. B., Pritzl, B. J., Smith, H. A., Kinemuchi, K., Layden, A. C., Sweigart, A. V., & Rich, R. M. 2006, *ApJ*, 651, L133
- Clark, G. W. 1975, *ApJ*, 199, L143
- Cohn, H. N., et al. 2010, *ApJ*, 722, 20
- Cseh, D., Kaaret, P., Corbel, S., Körding, E., Coriat, M., Tzioumis, A., & Lanzoni, B. 2010, *MNRAS*, 406, 1049

- Dalessandro, E., Lanzoni, B., Ferraro, F. R., Rood, R. T., Milone, A., Piotto, G., & Valenti, E. 2008, *ApJ*, 677, 1069
- Edmonds, P. D., Gilliland, R. L., Heinke, C. O., & Grindlay, J. E. 2003a, *ApJ*, 596, 1177
- . 2003b, *ApJ*, 596, 1197
- Elsner, R. F., et al. 2008, *ApJ*, 687, 1019
- Fabian, A. C., Pringle, J. E., & Rees, M. J. 1975, *MNRAS*, 172, 15P
- Fregeau, J. M. 2008, *ApJ*, 673, L25
- Fridriksson, J. K., et al. 2010, *ApJ*, 714, 270
- Giacconi, R., et al. 2001, *ApJ*, 551, 624
- Gregory, P. C., & Loredo, T. J. 1992, *ApJ*, 398, 146
- Grindlay, J. E., Camilo, F., Heinke, C. O., Edmonds, P. D., Cohn, H., & Lugger, P. 2002, *ApJ*, 581, 470
- Haggard, D., Cool, A. M., & Davies, M. B. 2009, *ApJ*, 697, 224
- Harris, W. E. 1996, *AJ*, 112, 1487
- Heinke, C. O., Grindlay, J. E., Edmonds, P. D., Cohn, H. N., Lugger, P. M., Camilo, F., Bogdanov, S., & Freire, P. C. 2005, *ApJ*, 625, 796
- Heinke, C. O., Grindlay, J. E., Lugger, P. M., Cohn, H. N., Edmonds, P. D., Lloyd, D. A., & Cool, A. M. 2003, *ApJ*, 598, 501
- Heinke, C. O., Wijnands, R., Cohn, H. N., Lugger, P. M., Grindlay, J. E., Pooley, D., & Lewin, W. H. G. 2006, *ApJ*, 651, 1098

- Hills, J. G. 1976, MNRAS, 175, 1P
- Ivanova, N., Heinke, C. O., Rasio, F. A., Belczynski, K., & Fregeau, J. M. 2008, MNRAS, 386, 553
- Ivanova, N., Heinke, C. O., Rasio, F. A., Taam, R. E., Belczynski, K., & Fregeau, J. 2006, MNRAS, 372, 1043
- Lanzoni, B., Dalessandro, E., Ferraro, F. R., Miocchi, P., Valenti, E., & Rood, R. T. 2007, ApJ, 668, L139
- Liedahl, D. A., Osterheld, A. L., & Goldstein, W. H. 1995, ApJ, 438, L115
- Lugger, P. M., Cohn, H., Grindlay, J. E., Bailyn, C. D., & Hertz, P. 1987, ApJ, 320, 482
- Lugger, P. M., Cohn, H. N., Heinke, C. O., Grindlay, J. E., & Edmonds, P. D. 2007, ApJ, 657, 286
- Lützgendorf, N., Kissler-Patig, M., Noyola, E., Jalali, B., de Zeeuw, P. T., Gebhardt, K., & Baumgardt, H. 2011, A&A, 533, A36
- Maccarone, T. J., & Peacock, M. B. 2011, MNRAS, 415, 1875
- Miocchi, P. 2007, MNRAS, 381, 103
- Noyola, E., & Gebhardt, K. 2006, AJ, 132, 447
- Nucita, A. A., de Paolis, F., Ingrosso, G., Carpano, S., & Guainazzi, M. 2008, A&A, 478, 763
- Nucita, A. A., De Paolis, F., Saxton, R., & Read, A. M. 2012, New A, 17, 589
- Pooley, D., Homan, J., Heinke, C. O., Sivakoff, G. R., Altamirano, D., Maxwell, J. E., Cohn, H., & Lugger, P. 2011, The Astronomer's Telegram, 3627, 1

- Pooley, D., & Hut, P. 2006, *ApJ*, 646, L143
- Pooley, D., et al. 2003, *ApJ*, 591, L131
- Revnivtsev, M., Sazonov, S., Gilfanov, M., Churazov, E., & Sunyaev, R. 2006, *A&A*, 452, 169
- Rich, R. M., et al. 1997, *ApJ*, 484, L25+
- Servillat, M., Webb, N. A., Lewis, F., Knigge, C., van den Berg, M., Dieball, A., & Grindlay, J. 2011, *ApJ*, 733, 106
- Shara, M. M., Bergeron, L. E., Gilliland, R. L., Saha, A., & Petro, L. 1996, *ApJ*, 471, 804
- Shara, M. M., Hinkley, S., & Zurek, D. R. 2005, *ApJ*, 634, 1272
- Sirianni, M., et al. 2005, *PASP*, 117, 1049
- Ushomirsky, G., & Rutledge, R. E. 2001, *MNRAS*, 325, 1157
- Verbunt, F. 1987, *ApJ*, 312, L23
- . 2001, *A&A*, 368, 137
- Verbunt, F. 2003, in *Astronomical Society of the Pacific Conference Series*, Vol. 296, *New Horizons in Globular Cluster Astronomy*, ed. G. Piotto, G. Meylan, S. G. Djorgovski, & M. Riello, 245
- Verbunt, F., & Hut, P. 1987, in *IAU Symp. 125: The Origin and Evolution of Neutron Stars*, 187
- Wallerstein, G., Kovtyukh, V. V., & Andrievsky, S. M. 2007, *AJ*, 133, 1373
- Zacharias, N., Urban, S. E., Zacharias, M. I., Wycoff, G. L., Hall, D. M., Monet, D. G., & Rafferty, T. J. 2004, *AJ*, 127, 3043

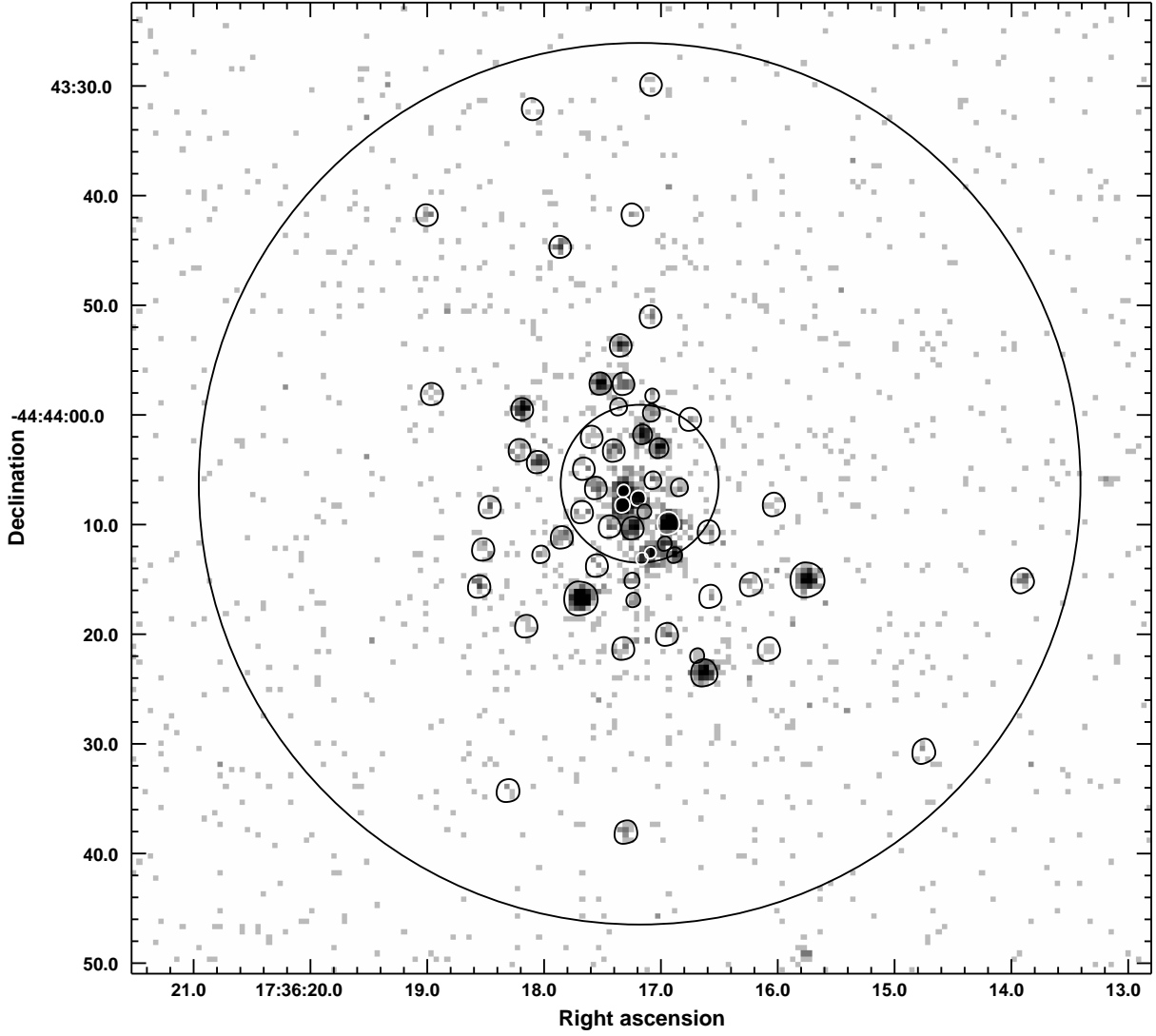


Fig. 1.— Chandra ACIS-S X-ray image of NGC 6388 (0.3-6 keV), with the core and half-mass radii indicated (7.2 arcsec and 0.67 arcminutes respectively, from Harris (1996), 2010 version), and the extraction regions for the sources within the half-mass radius of NGC 6388 marked.

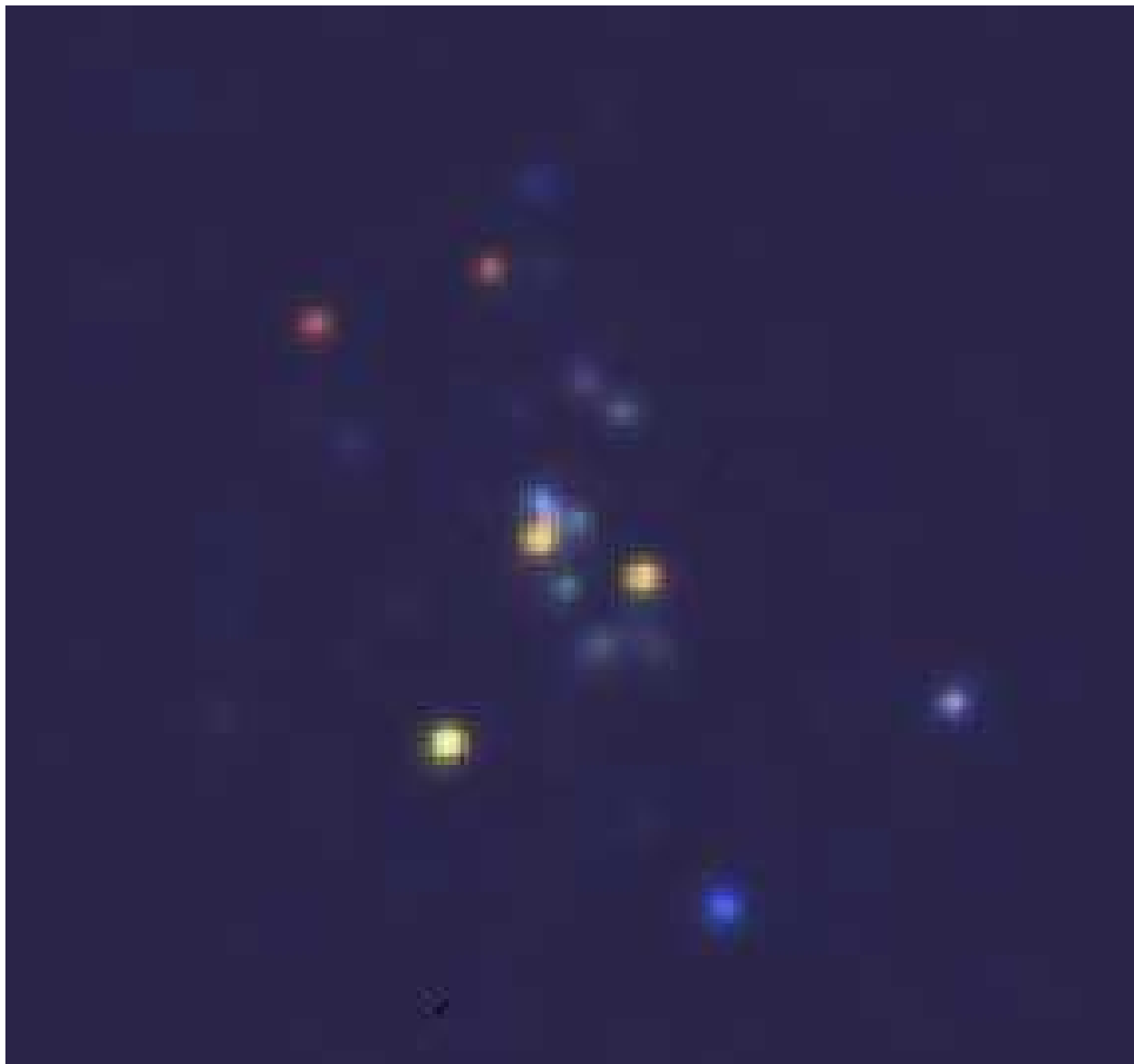


Fig. 2.— Representative color X-ray image of the central regions of NGC 6388 ($45'' \times 45''$). North is up and east is to the left. Images in 0.3-1.2 keV, 1.2-2 keV, and 2-6 keV were overbinned by a factor of 2, smoothed (using CIAO tool `csmooth`) using a $0.5''$ scale, and combined using the CIAO tool `dmimg2jpg`. Likely qLMXBs can be clearly identified by their yellow or red colors while the unusually blue color of CX4 stands out, at bottom right.

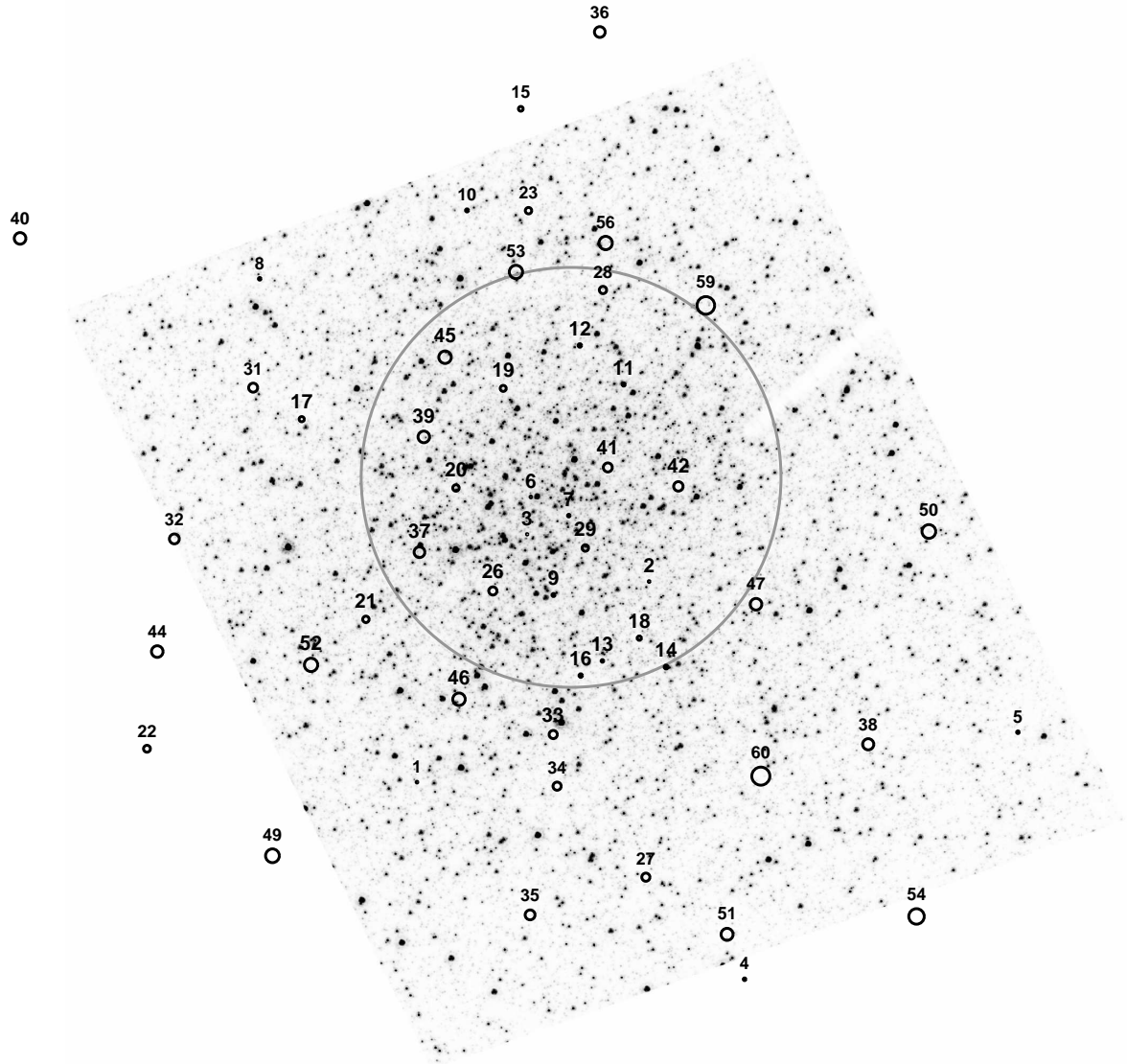


Fig. 3.— Positions of bore-sight corrected X-ray sources overlaid on the U_{330} image of NGC 6388 from 2006. North is up and east is to the left. Error circles are $1\text{-}\sigma$ errors from determination of X-ray source positions; no additional error is included. The large gray circle indicates the core radius of 7.2 arcsec.

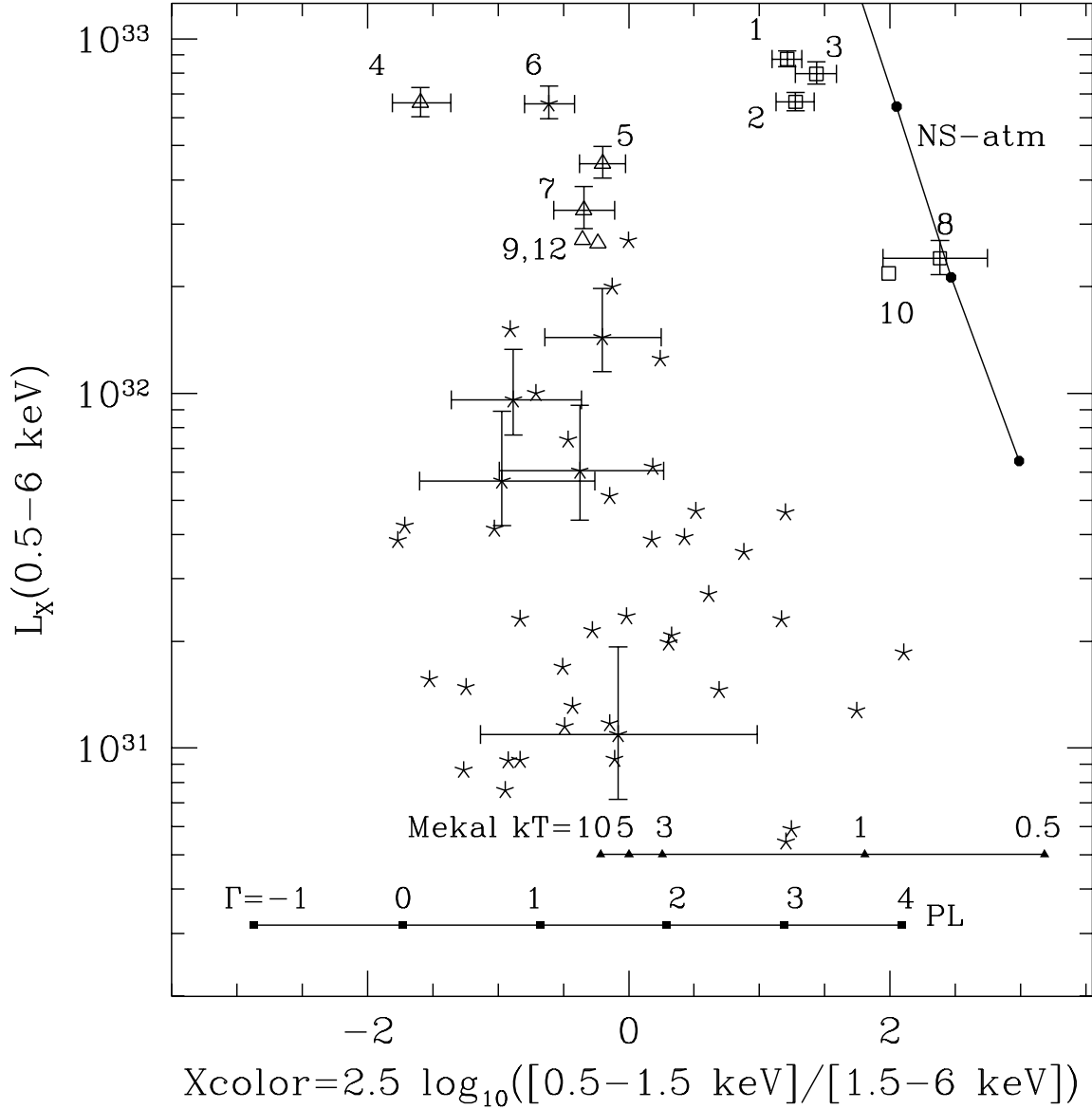


Fig. 4.— X-ray CMD of NGC 6388, plotting X-ray luminosity (0.5-6 keV, corrected for extinction of $N_H = 2.04 \times 10^{21} \text{ cm}^{-2}$) against an X-ray color for sources within the half-mass radius of NGC 6388. X-ray luminosities are computed using a 6 keV MEKAL spectrum, or an average of a MEKAL spectrum and a 10^6 K hydrogen-atmosphere NS spectrum, to convert photon fluxes into energy fluxes for each of 7 narrow bands, and summed. The open squares (colored red in the online version) indicate likely qLMXBs, and open triangles (colored blue in the online version) indicate CV candidates with optical counterparts (5,7,9, and 12) or identified from X-ray properties (4).

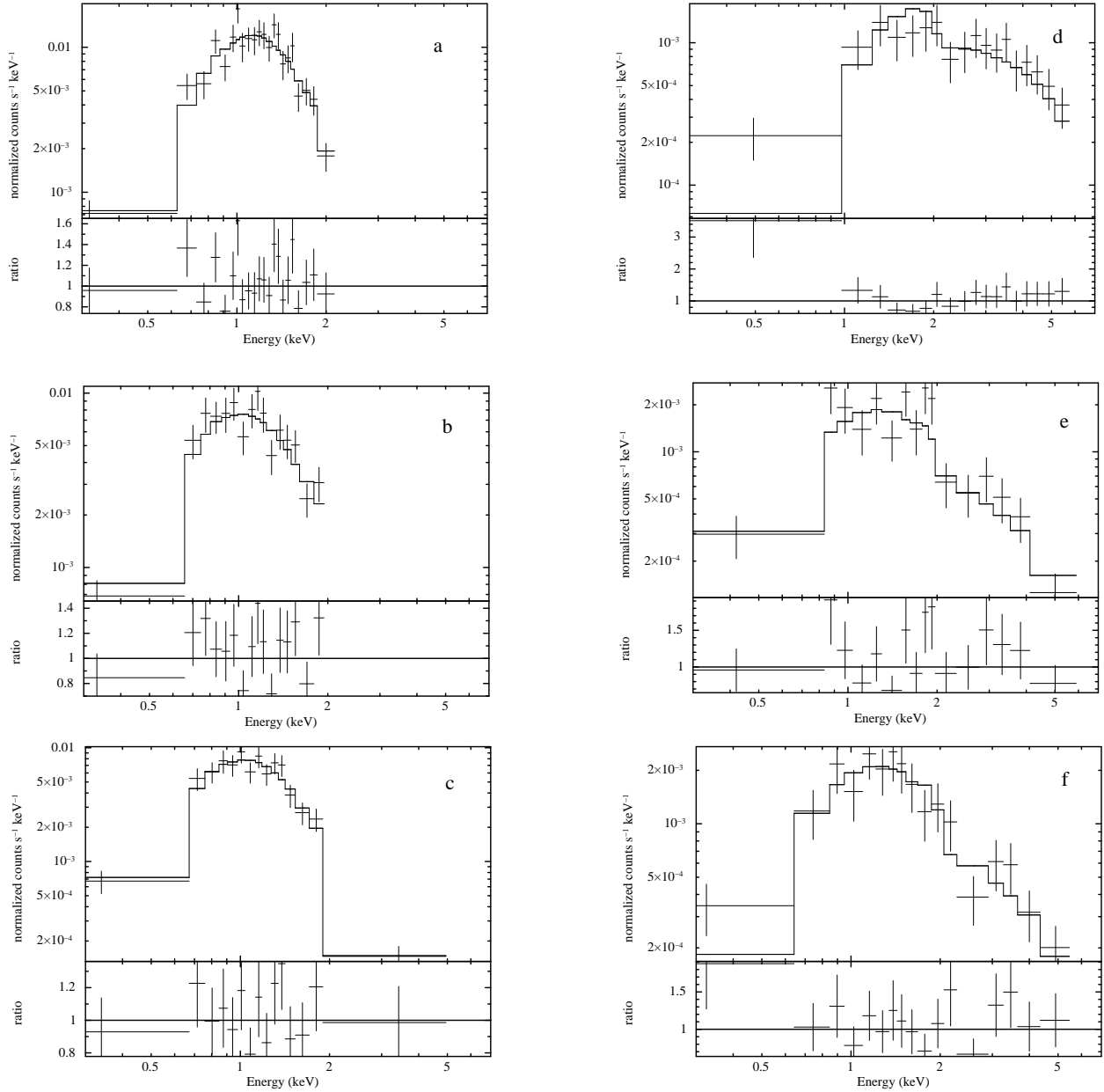


Fig. 5.— X-ray spectra (top, data; below, ratio of data/model) of six of the brightest X-ray sources in NGC 6388 (a: CX1; b: CX2; c: CX3; d: CX4; e: CX6; f: CX5). We show here binned (>10 counts/bin) spectra, though our reported spectral fits use the unbinned data and the C-statistic. Sources CX1, CX2, and CX3, which we argue are quiescent LMXBs, are plotted with absorbed NSATMOS+ power-law fits. Sources CX4, CX5, and CX6 are plotted with absorbed MEKAL fits. Note that CX4 shows an excess at low energies, arguing for a partial covering model.

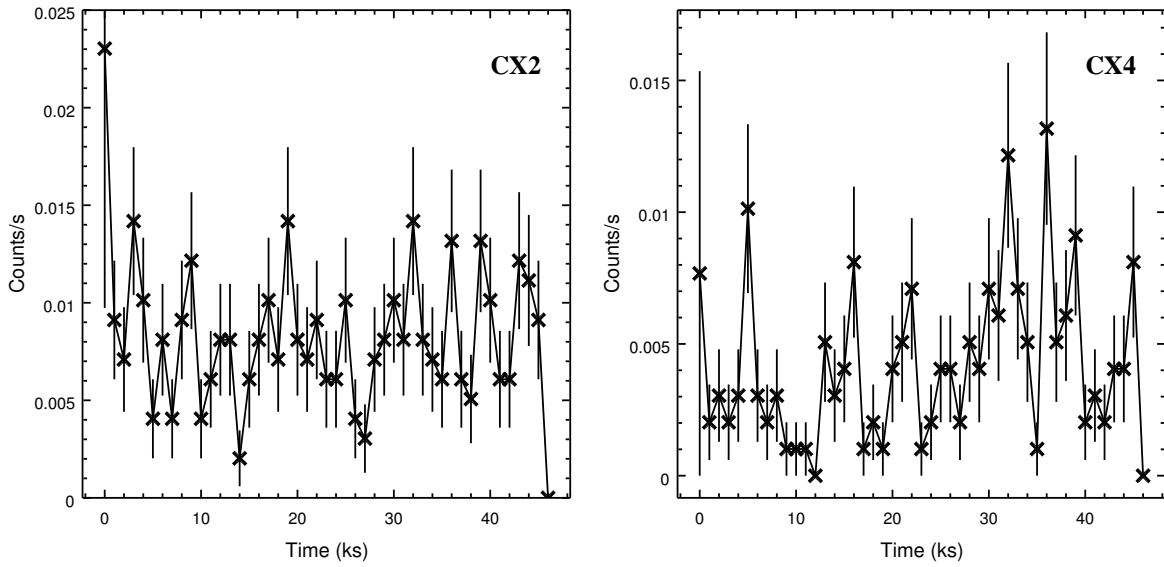


Fig. 6.— X-ray light curves for 2 sources, where one source (CX4) shows variation and the other (CX2) does not. CX4 is found to vary using the glvray package in CIAO with odds ratio $10^{-1.3}$ and probability 0.043.

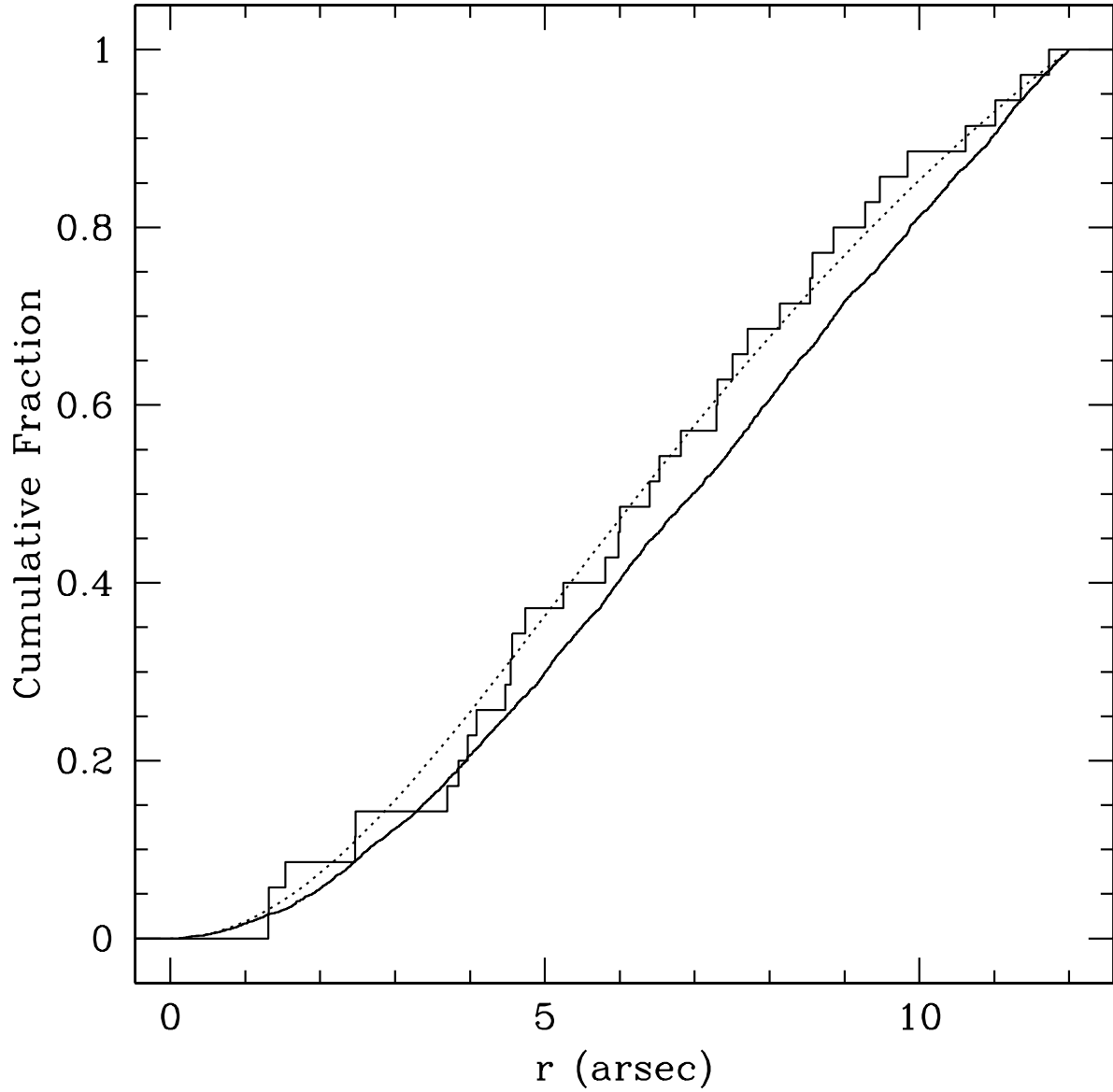


Fig. 7.— Comparison of the radial distribution of stars brighter than $V=20$ (the nearly smooth line) with that of all the X-ray sources. The best-fit generalized King model for the X-ray sources is shown by the dotted curve (colored red in the online version).

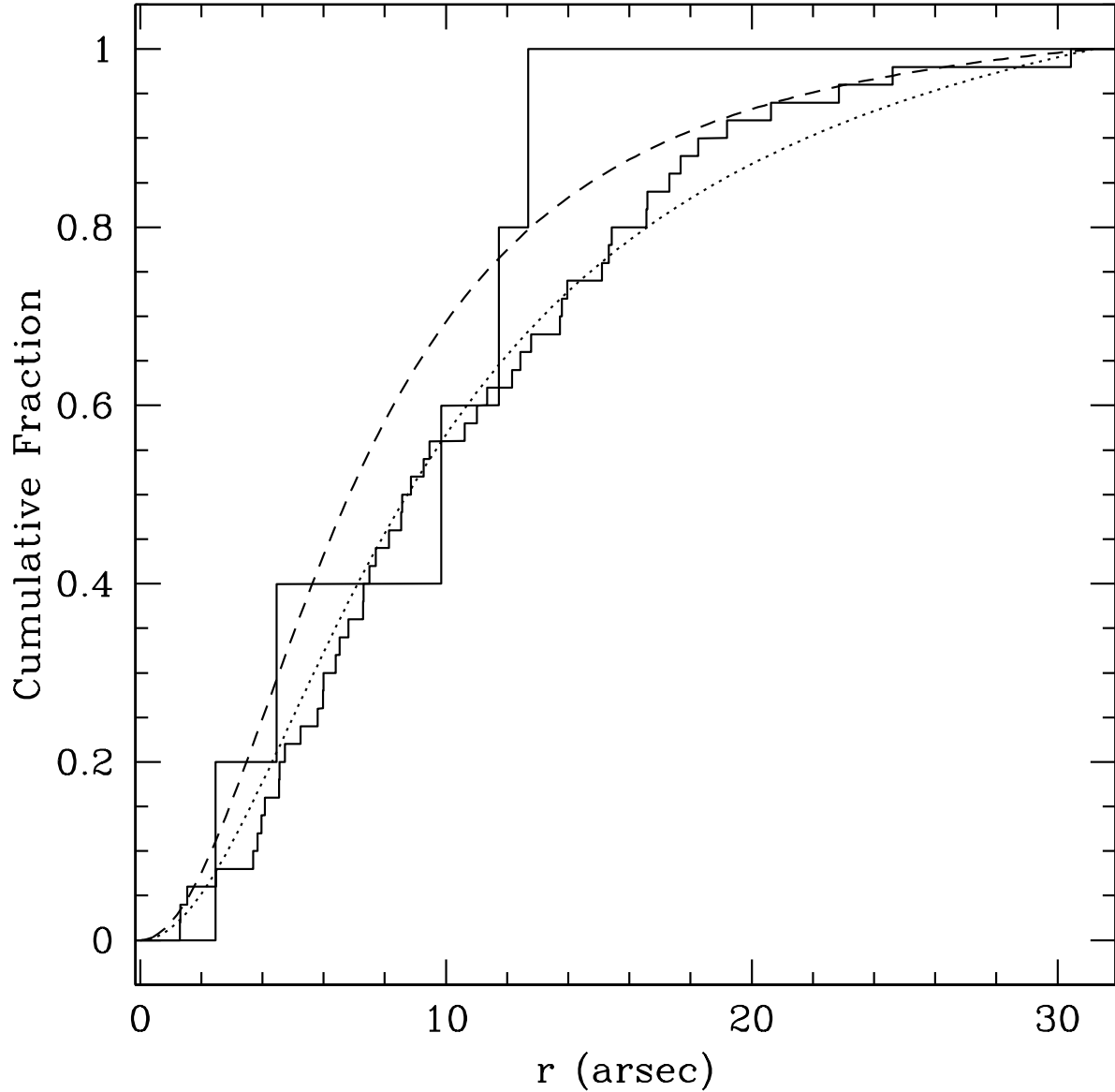


Fig. 8.— Comparison of the radial distribution for non-qLMXBs X-ray sources (the more complete distribution curve) vs. qLMXBs identified in this paper. For each distribution, we plot the best-fit generalized King model: dotted for the non-qLMXBs and dashed for the qLMXBs (colored red and green, respectively, in the online version).

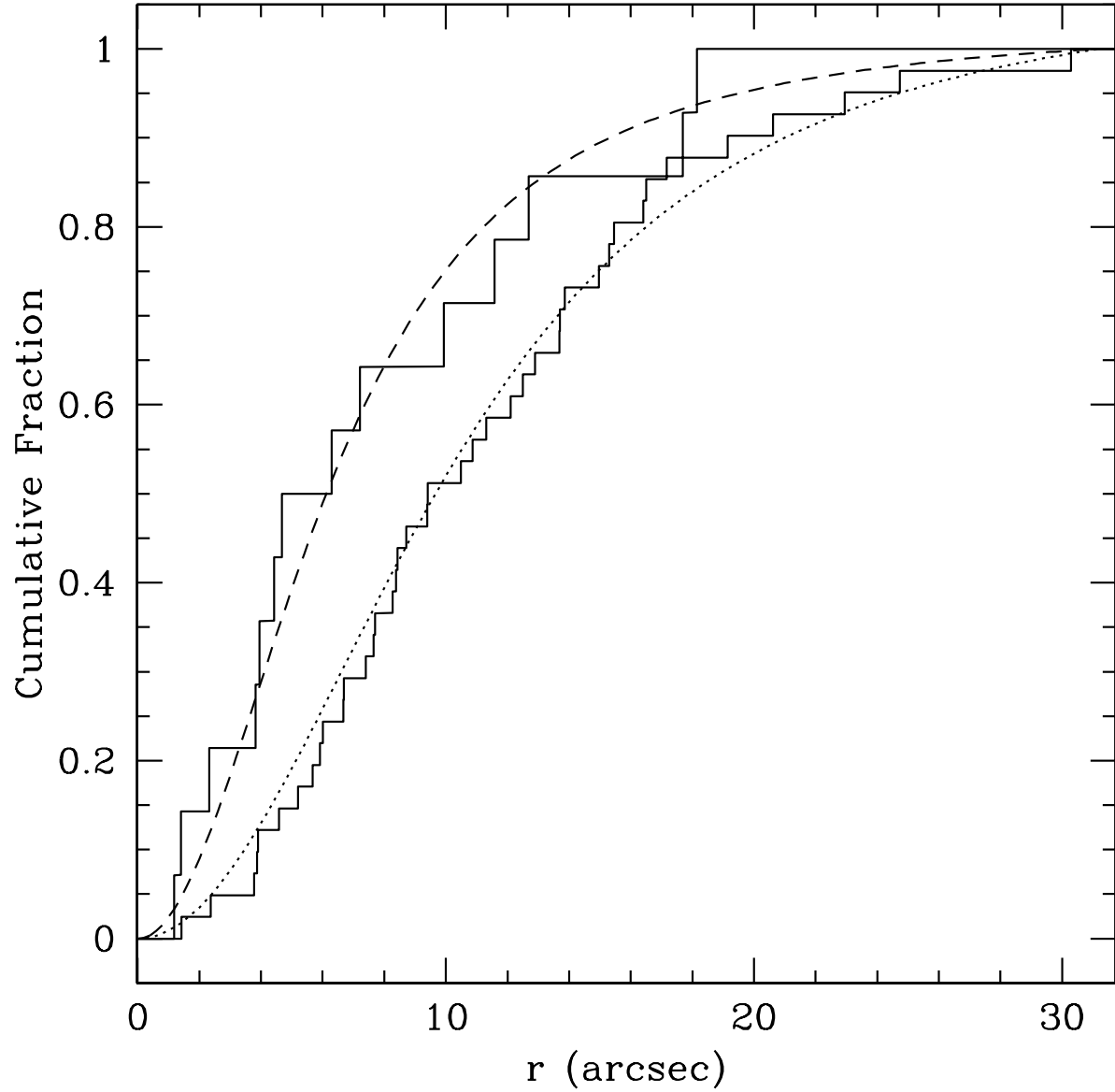


Fig. 9.— Comparison of the radial distribution for X-rays sources with counts > 40 vs. those with counts < 40 . For each distribution, we plot the best-fit generalized King model: dotted for the faint sources and dashed for the bright sources (colored red and green, respectively, in the online version).

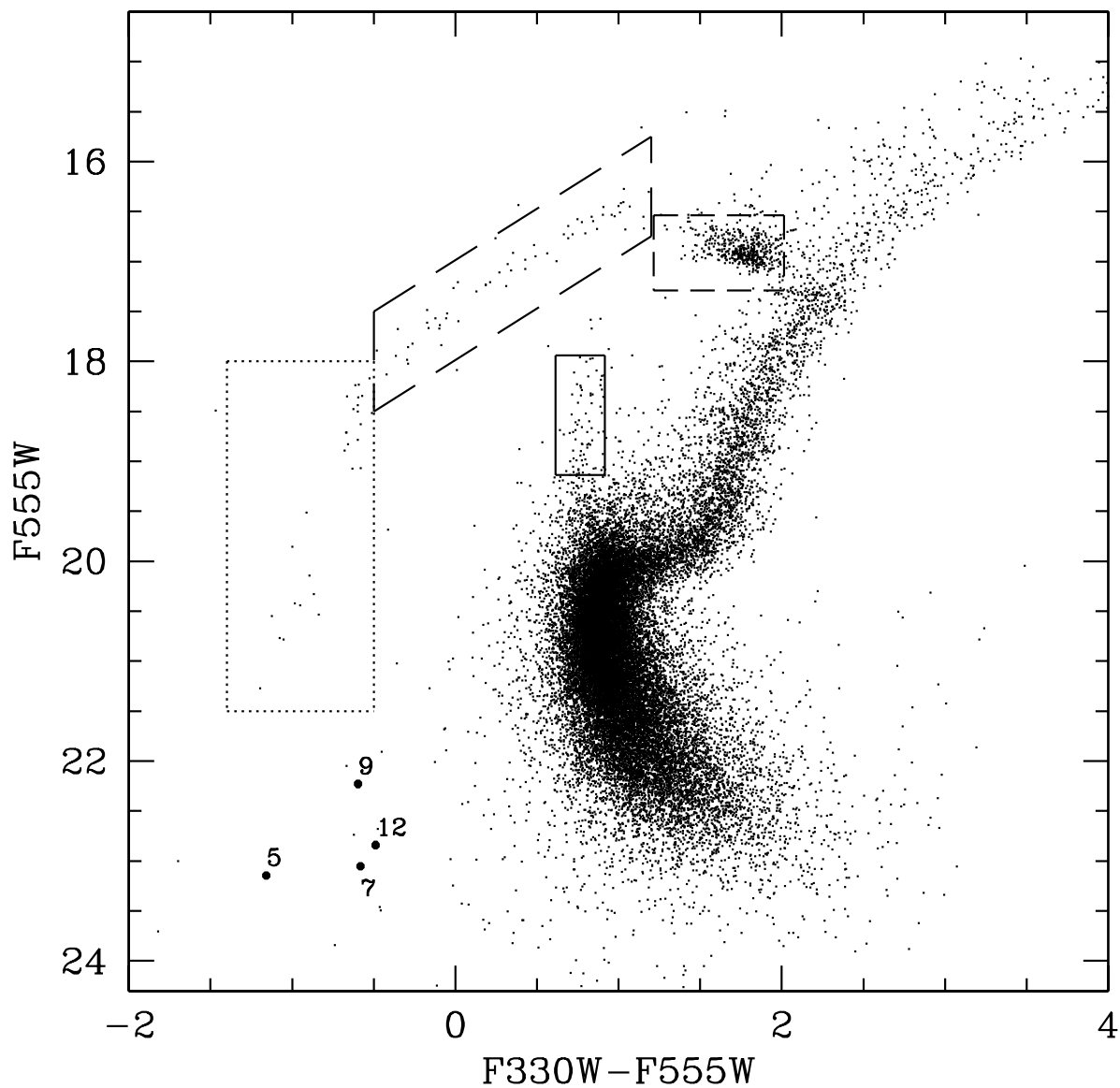


Fig. 10.— CMD for NGC 6388 with 4 optical counterparts labeled by their CX designations as used in this paper. The four stellar populations we compare in table 5 and fit in table 6 are outlined by the limits used for those populations: RHB (short dashed, colored red in the online version); BHB (long dashed, colored blue in the online version); EBHB (dotted, colored cyan in the online version); and BS sequence (solid, colored magenta in the online version).

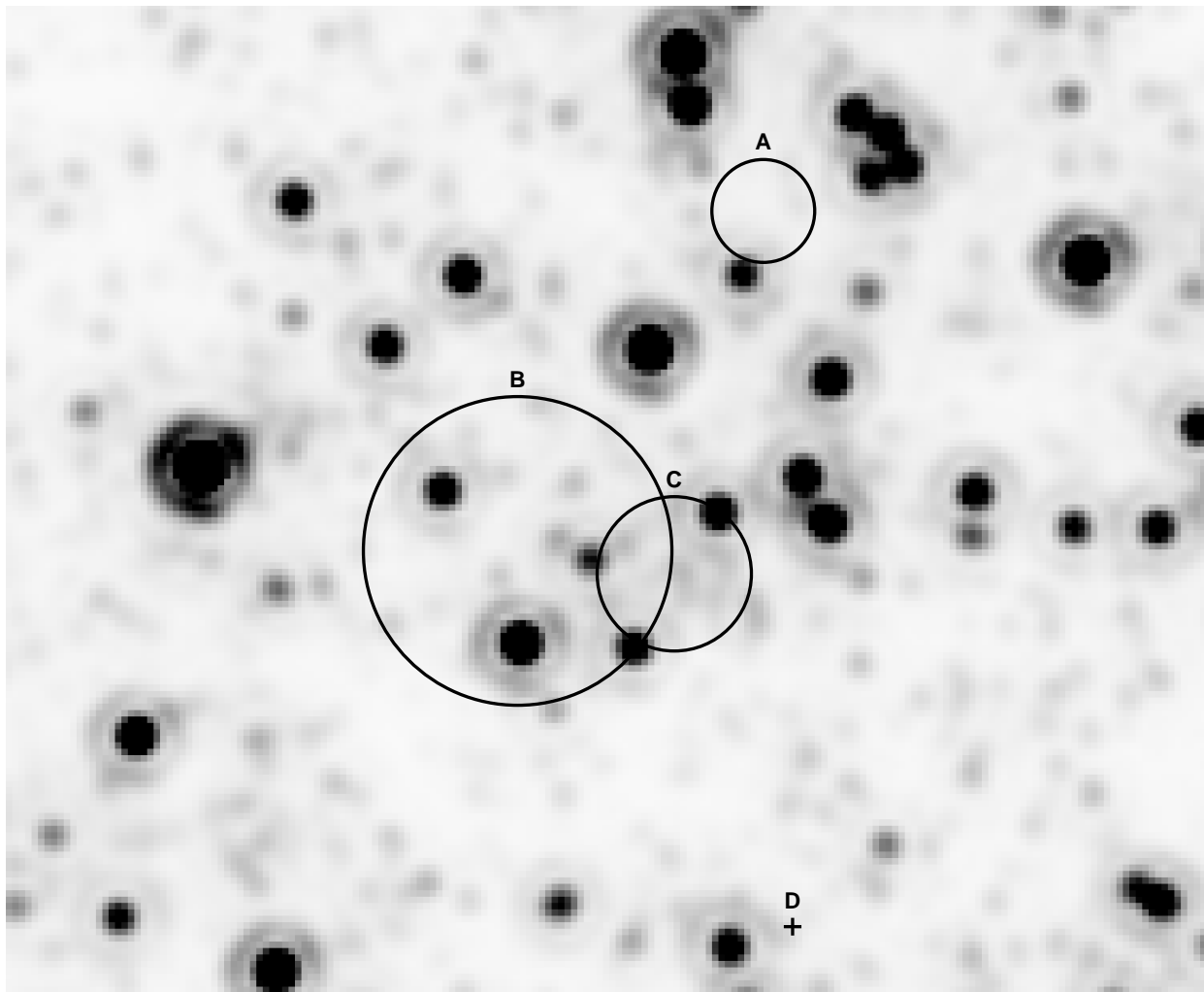


Fig. 11.— Finding chart for the center of NGC 6388 in the V_{555} filter. Error circles are $1\text{-}\sigma$ errors on the positions as reported by the authors of A: this research, B Lanzoni et al. (2007), and C: Lützendorf et al. (2011). For the center labeled D from Noyola & Gebhardt (2006), no error was given by the authors.

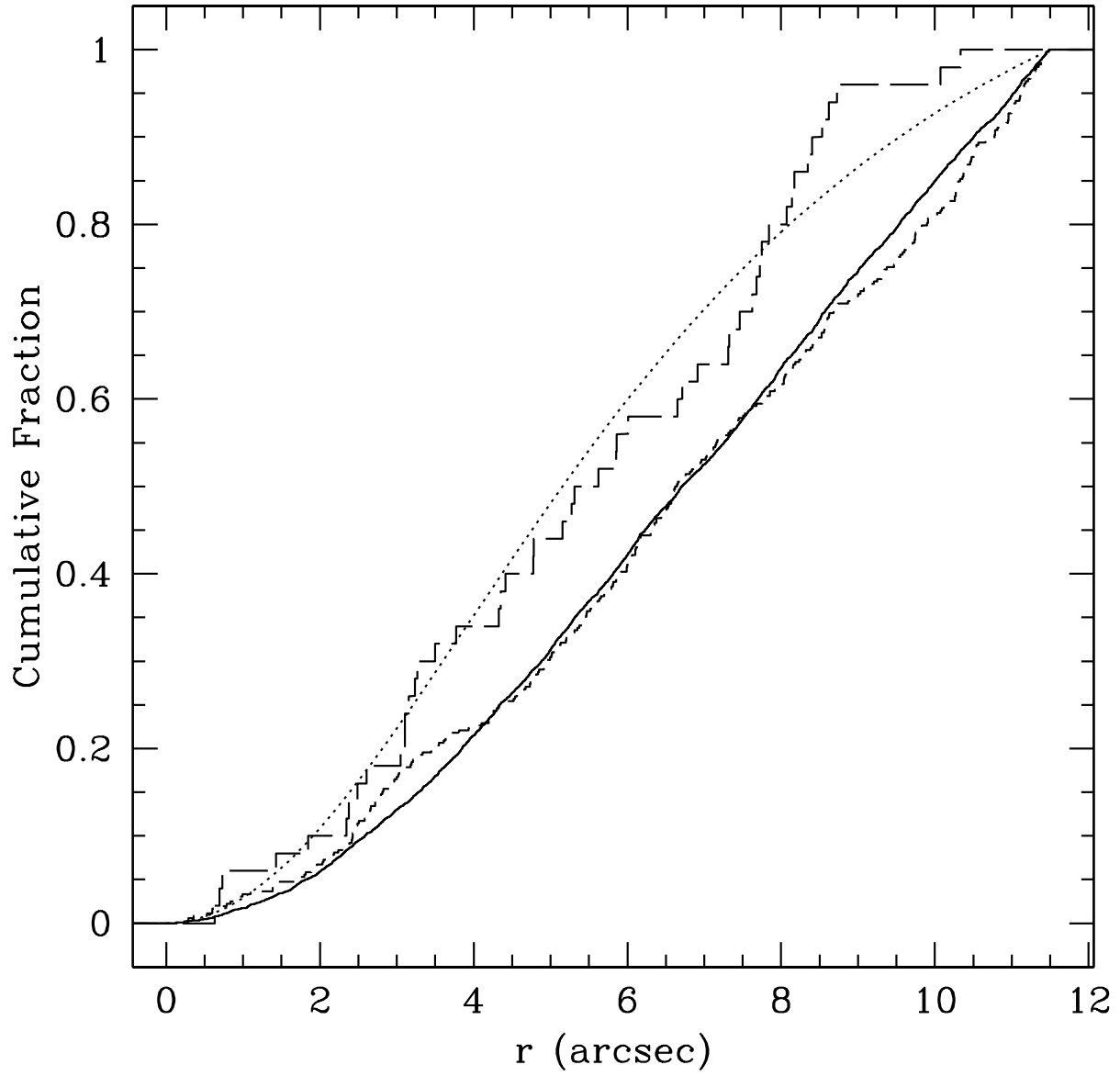


Fig. 12.— The radial distribution of three different stellar populations. The stars brighter than $V=20$ are depicted by the solid curve, the RHB stars by the short dashed curve and the blue stragglers by the long dashed curve. For the BS, we plot the best-fit generalized King model (dotted, colored red in the online version). Note how the RHB distribution is indistinguishable from that of the bright stars, while the BS distribution stands out as being more centrally concentrated.

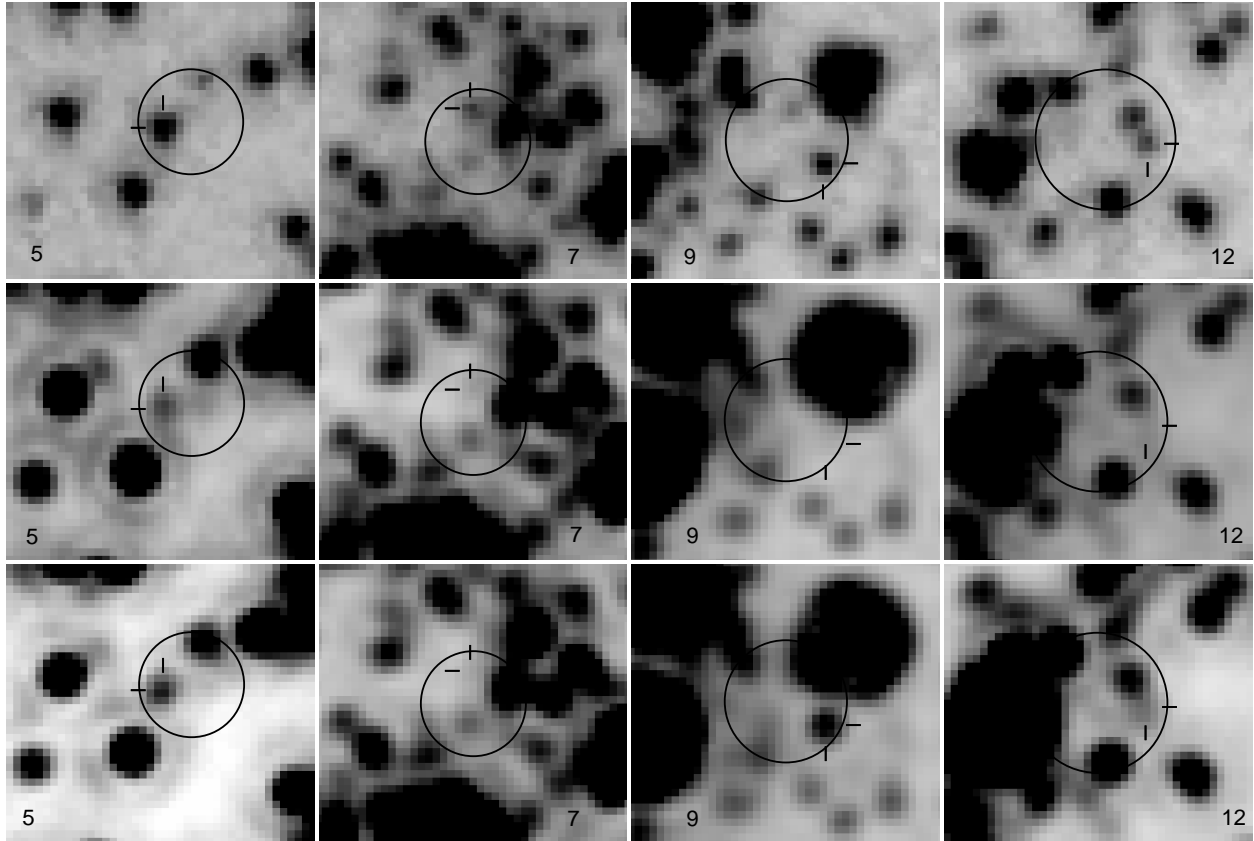


Fig. 13.— The finding charts for the four identified optical counterparts. We show the F330W from 2006 on the top row, F555W image from 2006 on the middle row, and F555W image from 2003 on the bottom row. The circles represent two times the 68% confidence regions for the positions of the X-ray sources. The counterparts are noted by the tick marks.

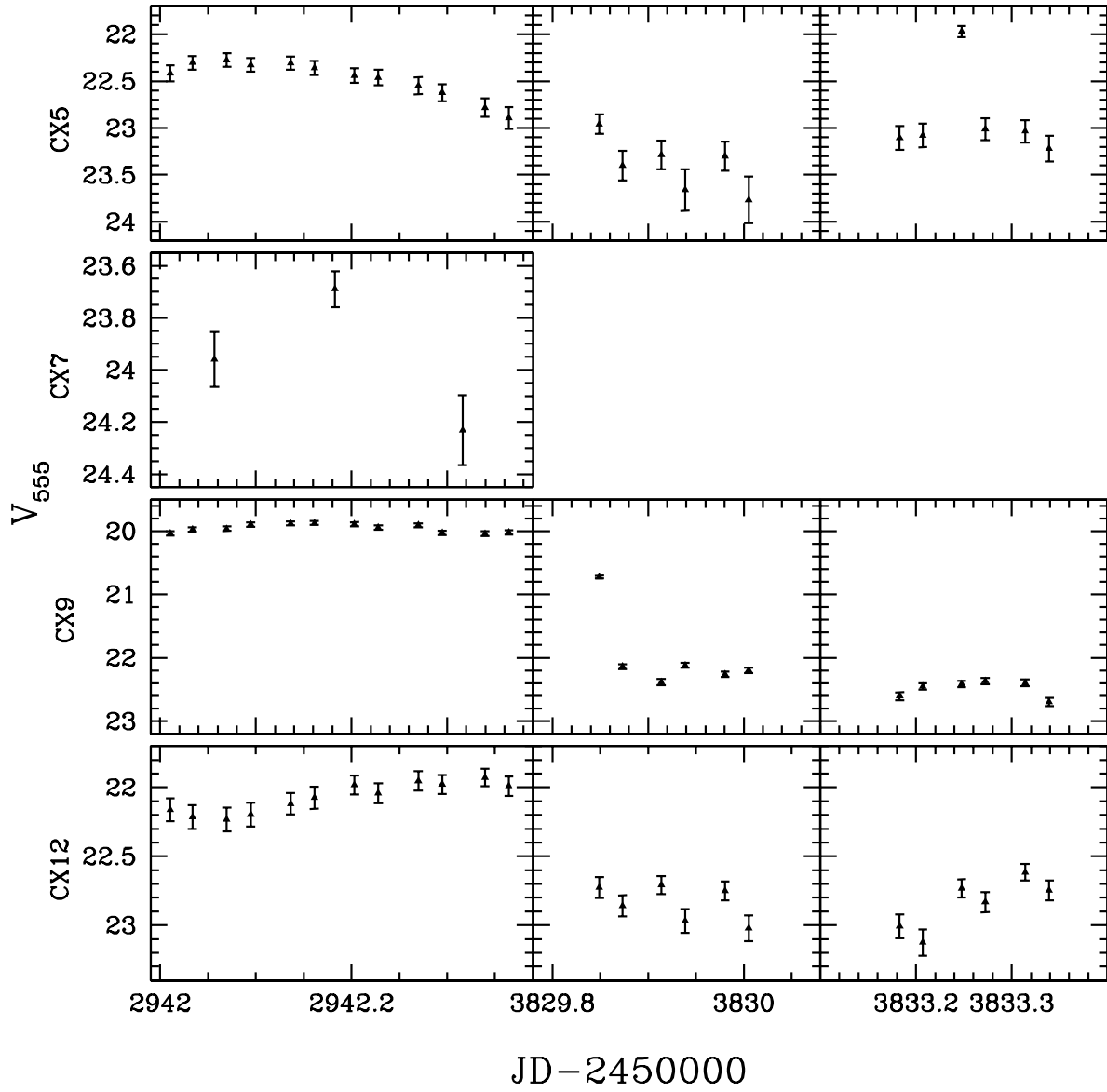


Fig. 14.— Light curves with $1\text{-}\sigma$ photometric error for the counterparts CX5, CX7, CX9, and CX12 for 2003 and 2006, except in the case of CX7, which was too faint in 2006 for a light curve.

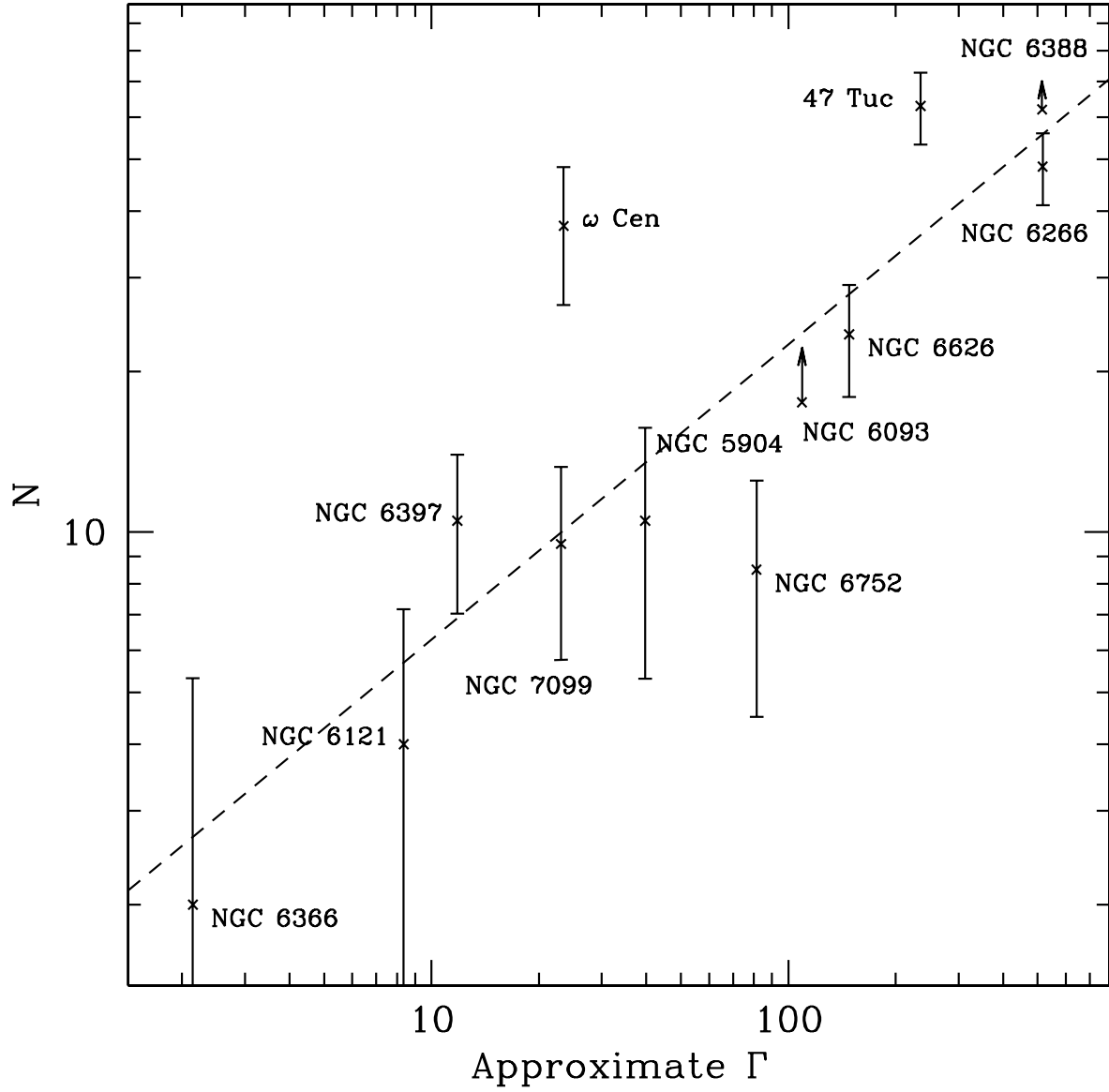


Fig. 15.— Plot of detected number of sources vs. the approximate values of Γ as given in Table 7. The source numbers are corrected for background contamination. The dashed line represents a least-squares power-law fit.

Table 1. *HST* Data Used in this Study.

Dataset	Date	Filter	Exposure Time
GO-9835	2003 Oct 30	F555W	48 × 155 s
GO-9835	2003 Oct 30	F814W	10 × 505 s
GO-9835	2003 Oct 30	F814W	5 × 25 s
GO-9835	2003 Oct 30	F814W	2 × 469 s
GO-10474	2006 Apr 04/05	F555W	48 × 155 s
GO-10474	2006 Apr 04/05	F814W	8 × 501 s
GO-10474	2006 Apr 04/05	F814W	4 × 25 s
GO-10474	2006 Apr 04/05	F814W	4 × 508 s
GO-10350	2006 Apr 07	F555W	3 × 155 s
GO-10350	2006 Apr 07	F330W	2 × 1266 s
GO-10350	2006 Apr 07	F330W	4 × 1314 s

Note. — All images were captured with the High Resolution Channel on the Advanced Camera for Surveys.

Table 2. ST Photometry for Four Optical Counterparts

star	RA (J2000)	Dec (J2000)	U_{330} (2006)	V_{555} (2003)	V_{555} (2006)
5	$17^h36^m15.747^s$	$-44^\circ44'15.06''$	21.99 ± 0.02	22.48 ± 0.02	23.15 ± 0.02
7	$17^h36^m17.187^s$	$-44^\circ44'07.57''$	22.47 ± 0.08	23.97 ± 0.12	23.05 ± 0.31
9	$17^h36^m17.231^s$	$-44^\circ44'10.38''$	21.63 ± 0.02	19.95 ± 0.01	22.23 ± 0.06
12	$17^h36^m17.142^s$	$-44^\circ44'01.79''$	22.35 ± 0.04	22.07 ± 0.02	22.84 ± 0.08

Table 3. X-ray Sources in NGC 6388

	Source	RA	Dec	Distance	Counts		L_X , ergs s ⁻¹		Notes
(CX)	(CXOGLB J)	(HH:MM:SS Err)	(DD:MM:SS Err)	($''$)	(0.5-1.5)	(1.5-6)	(0.5-6)	(0.5-2.5)	
1	173617.6-444416	17:36:17.686 0.002	-44:44:16.72 0.02	9.86	396.0 ^{+21.3} _{-19.9}	129.5 ^{+13.3} _{-11.3}	876.5 ^{+47.1} _{-41.2}	842.9 ^{+43.9} _{-39.9}	q
2	173616.9-444409	17:36:16.937 0.002	-44:44:09.85 0.02	3.42	268.5 ^{+17.8} _{-16.4}	82.8 ^{+11.1} _{-9.0}	663.7 ^{+43.0} _{-37.9}	650.2 ^{+41.6} _{-37.4}	q
3	173617.3-444408	17:36:17.329 0.001	-44:44:08.23 0.02	1.16	258.8 ^{+17.5} _{-16.1}	68.9 ^{+10.5} _{-8.2}	796.8 ^{+66.1} _{-51.2}	700.6 ^{+47.4} _{-42.3}	q
4	173616.6-444423	17:36:16.633 0.003	-44:44:23.48 0.03	16.50	34.6 ^{+7.4} _{-5.8}	150.5 ^{+14.6} _{-12.2}	660.0 ^{+69.6} _{-57.0}	147.8 ^{+21.9} _{-17.2}	c*
5	173615.7-444415	17:36:15.751 0.003	-44:44:15.02 0.03	17.06	79.1 ^{+10.4} _{-8.9}	95.2 ^{+12.1} _{-9.7}	444.4 ^{+52.4} _{-40.1}	213.2 ^{+24.9} _{-20.4}	c
6	173617.3-444406	17:36:17.317 0.002	-44:44:06.95 0.02	1.67	59.9 ^{+9.2} _{-7.7}	104.9 ^{+12.6} _{-10.2}	655.0 ^{+81.0} _{-60.5}	315.3 ^{+37.9} _{-30.8}	c
7	173617.1-444407	17:36:17.195 0.003	-44:44:07.59 0.03	0.68	45.8 ^{+8.3} _{-6.7}	62.9 ^{+10.3} _{-7.8}	328.6 ^{+54.1} _{-36.8}	173.9 ^{+26.4} _{-20.5}	c
8	173618.1-444359	17:36:18.188 0.003	-44:43:59.47 0.03	13.53	97.7 ^{+11.4} _{-9.8}	10.9 ^{+5.9} _{-3.2}	240.6 ^{+29.2} _{-24.5}	240.6 ^{+29.2} _{-24.5}	q
9	173617.2-444410	17:36:17.245 0.003	-44:44:10.31 0.04	2.10	44.5 ^{+8.2} _{-6.6}	61.7 ^{+10.3} _{-7.7}	270.8 ^{+46.7} _{-32.6}	135.8 ^{+20.9} _{-16.0}	c
10	173617.5-444357	17:36:17.520 0.003	-44:43:57.13 0.04	11.54	86.6 ^{+10.8} _{-9.3}	13.8 ^{+6.1} _{-3.6}	218.1 ^{+28.2} _{-23.1}	214.5 ^{+26.8} _{-22.9}	q
11	173617.0-444403	17:36:17.017 0.003	-44:44:03.100 0.04	5.62	41.7 ^{+8.0} _{-6.4}	41.8 ^{+8.9} _{-6.3}	269.7 ^{+54.8} _{-36.9}	128.7 ^{+23.0} _{-17.1}	c?
12	173617.1-444401	17:36:17.158 0.004	-44:44:01.76 0.04	6.48	33.7 ^{+7.3} _{-5.7}	41.8 ^{+9.0} _{-6.3}	264.9 ^{+54.1} _{-37.2}	112.3 ^{+22.4} _{-16.5}	c
13	173617.0-444412	17:36:17.088 0.003	-44:44:12.57 0.03	4.58	24.9 ^{+6.5} _{-4.9}	27.9 ^{+7.8} _{-5.1}	199.5 ^{+59.6} _{-34.6}	109.5 ^{+25.5} _{-17.4}	
14	173616.8-444412	17:36:16.883 0.004	-44:44:12.78 0.05	5.81	24.8 ^{+6.5} _{-4.9}	19.8 ^{+7.0} _{-4.3}	125.1 ^{+40.1} _{-20.8}	83.7 ^{+20.5} _{-14.3}	
15	173617.3-444353	17:36:17.346 0.005	-44:43:53.65 0.06	14.62	11.6 ^{+5.0} _{-3.3}	26.7 ^{+7.7} _{-5.0}	151.4 ^{+45.4} _{-29.2}	53.7 ^{+17.0} _{-11.2}	
16	173617.1-444413	17:36:17.158 0.004	-44:44:13.07 0.04	4.93	14.9 ^{+5.5} _{-3.8}	17.9 ^{+6.9} _{-4.0}	144.0 ^{+53.4} _{-29.0}	66.2 ^{+22.4} _{-14.3}	
17	173618.0-444404	17:36:18.054 0.006	-44:44:04.28 0.06	9.73	9.6 ^{+4.8} _{-3.0}	21.8 ^{+7.2} _{-4.5}	95.9 ^{+37.2} _{-19.7}	53.5 ^{+17.0} _{-11.1}	

Table 3—Continued

	Source	RA	Dec	Distance	Counts		L_X , ergs s ⁻¹		Notes
(CX)	(CXOGLB J)	(HH:MM:SS Err)	(DD:MM:SS Err)	(")	(0.5-1.5)	(1.5-6)	(0.5-6)	(0.5-2.5)	
18	173616.9-444411	17:36:16.969 0.005	-44:44:11.79 0.05	4.43	9.8 ^{+4.8} _{-3.0}	18.9 ^{+6.9} _{-4.1}	100.1 ^{+42.0} _{-20.9}	43.1 ^{+16.8} _{-9.8}	
19	173617.4-444403	17:36:17.405 0.007	-44:44:03.23 0.07	5.36	9.6 ^{+4.7} _{-3.0}	14.8 ^{+6.5} _{-3.7}	74.0 ^{+26.1} _{-15.6}	30.9 ^{+14.6} _{-8.2}	
20	173617.5-444406	17:36:17.558 0.007	-44:44:06.64 0.08	3.94	11.6 ^{+5.0} _{-3.3}	9.8 ^{+5.9} _{-2.9}	62.1 ^{+32.9} _{-15.0}	28.7 ^{+12.2} _{-7.5}	
21	173617.8-444411	17:36:17.849 0.007	-44:44:11.14 0.08	7.32	12.5 ^{+5.2} _{-3.4}	7.8 ^{+5.5} _{-2.6}	46.6 ^{+17.5} _{-10.6}	29.7 ^{+13.1} _{-7.7}	
22	173618.5-444415	17:36:18.555 0.008	-44:44:15.57 0.08	16.05	11.6 ^{+5.0} _{-3.3}	7.8 ^{+5.6} _{-2.6}	39.3 ^{+19.2} _{-9.3}	26.6 ^{+12.2} _{-6.5}	
23	173617.3-444357	17:36:17.322 0.007	-44:43:57.14 0.08	11.12	5.6 ^{+4.1} _{-2.2}	13.7 ^{+6.4} _{-3.5}	56.6 ^{+32.4} _{-14.3}	23.9 ^{+12.6} _{-6.3}	
24	173617.8-444344	17:36:17.863 0.008	-44:43:44.67 0.08	24.52	7.6 ^{+4.4} _{-2.6}	10.8 ^{+6.0} _{-3.1}	60.5 ^{+32.2} _{-16.5}	19.2 ^{+10.1} _{-5.7}	
25	173613.9-444415	17:36:13.911 0.009	-44:44:15.08 0.11	35.91	6.8 ^{+4.3} _{-2.5}	7.8 ^{+5.6} _{-2.5}	51.3 ^{+31.3} _{-15.0}	18.3 ^{+11.8} _{-6.1}	
26	173617.4-444410	17:36:17.440 0.009	-44:44:10.17 0.10	3.06	8.5 ^{+4.6} _{-2.8}	4.8 ^{+5.1} _{-2.0}	27.1 ^{+13.8} _{-7.6}	20.4 ^{+10.5} _{-6.2}	
27	173616.9-444419	17:36:16.950 0.009	-44:44:19.98 0.10	12.12	6.8 ^{+4.2} _{-2.5}	5.8 ^{+5.3} _{-2.2}	38.7 ^{+27.6} _{-12.3}	11.0 ^{+7.8} _{-3.8}	
28	173617.0-444359	17:36:17.083 0.008	-44:43:59.86 0.09	8.53	8.8 ^{+4.5} _{-2.8}	3.9 ^{+5.0} _{-1.7}	35.6 ^{+32.6} _{-12.1}	18.1 ^{+10.7} _{-5.3}	
29	173617.1-444408	17:36:17.142 0.007	-44:44:08.70 0.08	1.02	8.8 ^{+4.6} _{-2.8}	2.9 ^{+4.8} _{-1.4}	46.1 ^{+35.6} _{-14.6}	27.5 ^{+14.2} _{-8.9}	
30	173617.3-444438	17:36:17.300 0.010	-44:44:38.00 0.11	29.81	1.9 ^{+3.2} _{-1.3}	9.8 ^{+5.9} _{-2.9}	38.5 ^{+28.0} _{-12.0}	6.5 ^{+5.2} _{-2.7}	
31	173618.2-444403	17:36:18.210 0.010	-44:44:03.20 0.11	11.69	1.8 ^{+3.2} _{-1.2}	8.8 ^{+5.7} _{-2.7}	42.3 ^{+32.7} _{-15.1}	13.2 ^{+9.5} _{-5.0}	
32	173618.4-444408	17:36:18.465 0.011	-44:44:08.38 0.12	13.28	2.7 ^{+3.4} _{-1.4}	6.9 ^{+5.5} _{-2.4}	41.5 ^{+33.8} _{-13.9}	7.0 ^{+9.3} _{-3.3}	
33	173617.2-444415	17:36:17.247 0.009	-44:44:15.09 0.10	6.89	3.8 ^{+3.7} _{-1.8}	4.9 ^{+5.1} _{-2.0}	21.5 ^{+16.4} _{-6.9}	17.4 ^{+13.3} _{-6.0}	
34	173617.2-444416	17:36:17.235 0.009	-44:44:16.86 0.10	8.66	3.8 ^{+3.7} _{-1.8}	3.9 ^{+5.0} _{-1.6}	23.5 ^{+22.1} _{-8.0}	13.0 ^{+13.1} _{-4.9}	

Table 3—Continued

	Source	RA	Dec	Distance	Counts		L_X , ergs s ⁻¹		Notes
(CX)	(CXOGLB J)	(HH:MM:SS Err)	(DD:MM:SS Err)	($''$)	(0.5-1.5)	(1.5-6)	(0.5-6)	(0.5-2.5)	
35	173617.3-444421	17:36:17.323 0.011	-44:44:21.27 0.12	13.11	7.6 ^{+4.4} _{-2.6}	0.0 ^{+4.2} _{-0.0}	13.5 ^{+9.0} _{-5.0}	13.5 ^{+9.0} _{-5.0}	
36	173617.0-444351	17:36:17.091 0.012	-44:43:51.02 0.13	17.24	6.6 ^{+4.3} _{-2.4}	1.0 ^{+4.4} _{-0.8}	18.6 ^{+12.7} _{-6.6}	18.6 ^{+12.7} _{-6.6}	
37	173617.6-444408	17:36:17.676 0.012	-44:44:08.84 0.13	4.91	5.5 ^{+4.1} _{-2.2}	1.9 ^{+4.6} _{-1.1}	23.0 ^{+23.9} _{-9.4}	13.9 ^{+9.8} _{-5.4}	
38	173616.2-444415	17:36:16.233 0.012	-44:44:15.43 0.14	12.75	3.6 ^{+3.6} _{-1.7}	3.8 ^{+4.9} _{-1.9}	10.9 ^{+8.4} _{-3.7}	10.9 ^{+8.4} _{-3.7}	
39	173617.6-444404	17:36:17.661 0.013	-44:44:04.89 0.14	5.76	0.0 ^{+2.6} _{-0.0}	6.8 ^{+5.5} _{-2.3}	24.2 ^{+19.9} _{-9.0}	9.5 ^{+9.6} _{-4.6}	
40	173618.9-444358	17:36:18.959 0.013	-44:43:58.08 0.14	21.13	3.9 ^{+3.7} _{-1.9}	2.9 ^{+4.8} _{-1.4}	20.8 ^{+26.5} _{-9.6}	6.7 ^{+5.6} _{-2.8}	
41	173617.0-444405	17:36:17.069 0.010	-44:44:05.94 0.11	2.78	6.7 ^{+4.3} _{-2.5}	0.0 ^{+4.2} _{-0.0}	16.5 ^{+10.9} _{-6.4}	16.5 ^{+10.9} _{-6.4}	
42	173616.8-444406	17:36:16.842 0.010	-44:44:06.59 0.12	4.33	6.7 ^{+4.3} _{-2.4}	0.0 ^{+4.2} _{-0.0}	17.5 ^{+11.0} _{-6.7}	17.5 ^{+11.0} _{-6.7}	
43	173619.0-444341	17:36:19.002 0.013	-44:43:41.79 0.13	32.55	3.7 ^{+3.7} _{-1.8}	2.8 ^{+4.8} _{-1.4}	19.8 ^{+24.8} _{-8.8}	7.2 ^{+8.0} _{-3.0}	
44	173618.5-444412	17:36:18.521 0.013	-44:44:12.24 0.14	14.45	2.6 ^{+3.4} _{-1.4}	3.9 ^{+5.0} _{-1.7}	13.1 ^{+12.8} _{-4.7}	9.8 ^{+10.1} _{-3.7}	
45	173617.5-444402	17:36:17.592 0.014	-44:44:02.16 0.15	7.39	3.6 ^{+3.7} _{-1.7}	1.9 ^{+4.6} _{-1.1}	14.6 ^{+14.2} _{-5.6}	10.9 ^{+11.2} _{-4.7}	
46	173617.5-444413	17:36:17.550 0.014	-44:44:13.88 0.15	6.53	1.8 ^{+3.2} _{-1.2}	3.8 ^{+5.0} _{-1.6}	23.1 ^{+26.8} _{-9.6}	6.1 ^{+7.9} _{-3.5}	
47	173616.5-444410	17:36:16.593 0.013	-44:44:10.63 0.14	7.09	4.6 ^{+3.9} _{-2.0}	0.9 ^{+4.4} _{-0.8}	12.7 ^{+13.5} _{-5.3}	8.4 ^{+8.0} _{-3.8}	
48	173614.7-444430	17:36:14.769 0.016	-44:44:30.79 0.18	34.53	0.9 ^{+3.0} _{-0.8}	3.8 ^{+5.0} _{-1.7}	15.6 ^{+23.2} _{-8.2}	6.5 ^{+7.9} _{-3.0}	
49	173618.1-444419	17:36:18.152 0.015	-44:44:19.24 0.17	14.85	1.8 ^{+3.2} _{-1.2}	2.9 ^{+4.8} _{-1.4}	11.5 ^{+14.3} _{-5.1}	3.5 ^{+4.5} _{-1.8}	
50	173616.0-444408	17:36:16.036 0.015	-44:44:08.14 0.17	12.61	1.8 ^{+3.2} _{-1.2}	2.9 ^{+4.8} _{-1.5}	16.9 ^{+23.2} _{-8.6}	7.7 ^{+8.1} _{-3.8}	
51	173616.6-444421	17:36:16.689 0.013	-44:44:21.94 0.15	14.85	0.9 ^{+3.0} _{-0.8}	2.9 ^{+4.7} _{-1.6}	8.7 ^{+9.8} _{-4.0}	8.7 ^{+9.8} _{-4.0}	

Table 3—Continued

	Source	RA	Dec	Distance	Counts	L_X , ergs s ⁻¹		Notes
(CX)	(CXOGLB J)	(HH:MM:SS Err)	(DD:MM:SS Err)	(")	(0.5-1.5)	(1.5-6)	(0.5-6)	(0.5-2.5)
52	173618.0-444412	17:36:18.026 0.015	-44:44:12.70 0.16	9.70	2.9 ^{+3.5} _{-1.6}	1.0 ^{+4.4} _{-0.8}	5.4 ^{+5.4} _{-2.5}	5.4 ^{+5.4} _{-2.5}
53	173617.3-444359	17:36:17.363 0.015	-44:43:59.24 0.16	9.10	2.9 ^{+3.5} _{-1.6}	0.9 ^{+4.4} _{-0.8}	5.9 ^{+5.9} _{-2.7}	5.9 ^{+5.9} _{-2.7}
54	173616.0-444421	17:36:16.079 0.017	-44:44:21.33 0.19	17.88	0.9 ^{+2.9} _{-0.8}	2.8 ^{+4.8} _{-1.4}	14.8 ^{+23.7} _{-8.3}	2.3 ^{+4.3} _{-1.4}
55	173618.3-444434	17:36:18.308 0.018	-44:44:34.22 0.19	28.48	1.7 ^{+3.2} _{-1.1}	1.9 ^{+4.6} _{-1.1}	9.3 ^{+13.4} _{-4.6}	4.7 ^{+7.6} _{-2.5}
56	173617.0-444358	17:36:17.074 0.015	-44:43:58.25 0.16	10.08	0.9 ^{+2.9} _{-0.8}	1.9 ^{+4.6} _{-1.1}	9.2 ^{+13.5} _{-4.7}	9.2 ^{+13.5} _{-4.7}
57	173618.0-444332	17:36:18.099 0.019	-44:43:32.12 0.21	37.28	0.8 ^{+2.9} _{-0.7}	2.0 ^{+4.6} _{-1.3}	9.2 ^{+11.1} _{-4.9}	2.4 ^{+6.3} _{-2.1}
58	173617.2-444341	17:36:17.246 0.019	-44:43:41.74 0.21	26.47	2.7 ^{+3.4} _{-1.4}	0.0 ^{+4.2} _{-0.0}	4.5 ^{+7.0} _{-2.5}	4.5 ^{+7.0} _{-2.5}
59	173616.7-444400	17:36:16.752 0.019	-44:44:00.39 0.22	9.27	2.5 ^{+3.4} _{-1.4}	0.0 ^{+4.2} _{-0.0}	6.5 ^{+8.6} _{-3.8}	6.5 ^{+8.6} _{-3.8}
60	173616.5-444416	17:36:16.579 0.020	-44:44:16.52 0.22	10.75	0.7 ^{+2.9} _{-0.7}	1.8 ^{+4.6} _{-1.1}	7.6 ^{+12.9} _{-4.3}	3.2 ^{+6.9} _{-2.1}
61	173617.0-444329	17:36:17.088 0.019	-44:43:29.88 0.21	38.36	0.9 ^{+2.9} _{-0.7}	1.0 ^{+4.4} _{-0.8}	11.7 ^{+23.0} _{-8.1}	2.4 ^{+6.3} _{-2.1}

Note. — Names, positions, distance from center of NGC 6388, counts in two X-ray energy bands (energies given in keV), and estimated X-ray luminosities (in units of 10³⁰ ergs s⁻¹) of X-ray sources associated with NGC 6388. The errors after the position represent the 1 σ uncertainties in the relative positions of the sources, derived from ACIS_EXTRACT centroiding. The counts in each band are the numbers of photons within the source regions of Figure 1. Luminosities are computed from

the corrected photon fluxes in several narrow bands, see text. Notes indicate short-term variability ($V = 99\%$ confidence, $V? = 95\%$ confidence), years-timescale variability between 2000 and 2003 (Y), and possible identifications ($q = \text{qLMXB}$, $q? = \text{qLMXB candidate}$, $c = \text{CV with optical counterpart identified}$, $c^* = \text{CV identified from X-ray properties}$, $c? = \text{possible optical counterpart identification}$).

Table 4. Spectral Fits to Bright NGC 6388 Sources

CX	H-atmosphere + Power-law					MEKAL				Power-law			
	kT	N_H	PL	Good-	L_X	kT	N_H	Good-	L_X	α	N_H	Good-	L_X
(eV)	($\times 10^{21}$	(%)	(%)	($\times 10^{32}$	(keV)	($\times 10^{21}$	(%)	($\times 10^{32}$	($\times 10^{21}$	(%)	($\times 10^{32}$		
	cm $^{-2}$)			ergs s $^{-1}$)		cm $^{-2}$)		ergs s $^{-1}$)	cm $^{-2}$)		ergs s $^{-1}$)		
1	130 $^{+2}_{-2}$	4.0 $^{+0.4}_{-0.4}$	0 $^{+4}_{-0}$	51	15 $^{+1}_{-1}$	0.49	8.9	100	62	5.4 $^{+0.6}_{-0.5}$	8.6 $^{+0.1}_{-0.1}$	8	130 $^{+110}_{-50}$
2	119 $^{+3}_{-3}$	3.5 $^{+0.4}_{-0.4}$	0 $^{+7}_{-0}$	10	9.9 $^{+1.2}_{-1.2}$	1.3 $^{+0.1}_{-0.2}$	2.2 $^{+0.2}_{-0}$	13.4	6.7 $^{+0.6}_{-0.6}$	5.0 $^{+0.6}_{-0.6}$	6.8 $^{+1.3}_{-1.2}$	2.5	49 $^{+46}_{-21}$
3	117 $^{+4}_{-4}$	3.2 $^{+0.5}_{-0.5}$	18 $^{+11}_{-7}$	40	11.0 $^{+2.3}_{-2.0}$	1.1	2.2	95	7.3	4.5 $^{+0.7}_{-0.6}$	6.0 $^{+1.4}_{-1.3}$	79	37 $^{+36}_{-15}$
8	92 $^{+4}_{-4}$	2.5 $^{+0.5}_{-0.3}$	0 $^{+8}_{-0}$	72	3.0 $^{+0.6}_{-0.6}$	0.8 $^{+0.1}_{-0.1}$	2.2 $^{+0.4}_{-0}$	89	2.3 $^{+0.4}_{-0.3}$	6.6 $^{+1.9}_{-1.5}$	0.8 $^{+0.3}_{-0.3}$	24	5 $^{+29}_{-4}$
10	91 $^{+5}_{-4}$	2.7 $^{+0.7}_{-0.5}$	0 $^{+13}_{-0}$	6	2.8 $^{+0.7}_{-0.6}$	0.5 $^{+0.2}_{-0.3}$	3.9 $^{+5.0}_{-1.7}$	85	4.0 $^{+96}_{-2.0}$	6.2 $^{+1.9}_{-1.4}$	7.4 $^{+3.2}_{-2.5}$	9	30 $^{+170}_{-20}$
11	87 $^{+11}_{-20}$	5.5 $^{+2.0}_{-2.1}$	60 $^{+28}_{-23}$	21	5.5 $^{+0.7}_{-0.5}$	5.0 $^{+14}_{-2.3}$	2.7 $^{+1.6}_{-0.4}$	6	3.2 $^{+1.0}_{-0.7}$	2.0 $^{+0.6}_{-0.6}$	3.8 $^{+2.2}_{-1.6}$	14	3.8 $^{+1.2}_{-0.8}$
5	49 $^{+31}_{-49}$	2.2 $^{+1.8}_{-0}$	98 $^{+2}_{-21}$	72	6 $^{+1}_{-1}$	8.6 $^{+15}_{-3.8}$	2.2 $^{+6}_{-0}$	61	5.5 $^{+1.2}_{-0.9}$	1.6 $^{+4}_{-2}$	2.2 $^{+1.3}_{-0}$	59	5.9 $^{+1.2}_{-0.9}$
4	67 $^{+24}_{-67}$	10.2 $^{+3.3}_{-2.5}$	95 $^{+5}_{-14}$	41	13 $^{+4}_{-3}$	80	7.6	99	11.0	0.9 $^{+0.4}_{-0.4}$	5.0 $^{+3.4}_{-2.5}$	26	12 $^{+3}_{-2}$
7	< 96	2.5 $^{+4.3}_{-0.3}$	100 $^{+0}_{-45}$	3	5.1 $^{+2.6}_{-0.9}$	4.4 $^{+8.1}_{-1.8}$	3.1 $^{+1.6}_{-0.9}$	23	4.2 $^{+1.1}_{-0.8}$	2.0 $^{+0.6}_{-0.5}$	4.2 $^{+}_{-}$	24	5.1 $^{+1.6}_{-1.0}$
9	89 $^{+13}_{-24}$	6.7 $^{+2.4}_{-1.6}$	61 $^{+30}_{-33}$	8	6.4 $^{+3.6}_{-2.0}$	4.2 $^{+6.4}_{-1.7}$	4.0 $^{+1.8}_{-1.5}$	63	3.7 $^{+0.8}_{-0.8}$	2.2 $^{+0.6}_{-0.5}$	5.4 $^{+2.5}_{-2.1}$	29	4.6 $^{+1.8}_{-1.0}$
6	0 $^{+87}_{-0}$	2.8 $^{+0.9}_{-0.3}$	100 $^{+0}_{-22}$	31	9.9 $^{+2.7}_{-1.5}$	9.0 $^{+37}_{-4.7}$	2.7 $^{+1.2}_{-0.5}$	40	8.9 $^{+1.8}_{-0.9}$	1.6 $^{+0.4}_{-0.4}$	3.2 $^{+1.6}_{-1.0}$	18	9.7 $^{+1.8}_{-1.6}$

Note. — Spectral fits to sources with more than 80 counts. Errors are 90% confidence for one parameter of interest. The hydrogen column density (N_H) to the cluster is 2.2×10^{21} cm $^{-2}$, which was used as a lower bound. L_X in erg s $^{-1}$ for 0.5-10 keV, assuming distance of 10 kpc. Hydrogen atmosphere NS fits assume R=10 km, M=1.4 M_\odot NSs, while the power-law photon index was fixed to 1.5. “Goodness” is the fraction of simulations with a smaller C-statistic than the given spectral fit; large “goodness” values indicate a poor fit, for which no errors are provided.

Table 5. Population distribution comparisons.

compared pops	Prob.
Optical:	
RHB vs. 20 w/o	0.32
BS vs. 20 w/o	0.004
RHB vs. BHB	0.67
RHB vs. EBHB	0.96
BHB vs. EBHB	0.91
X-ray:	
non-qLMXB vs. qLMXB	0.48
bright vs. faint	0.09

Note. — The probability that the listed populations are drawn from the same underlying distribution as determined by a K-S test. ‘20’ signifies all stars with $V_{555} < 20$. ‘w/o’ specifies that the RHB or BS were removed from the ‘20’ sample before comparing to their respective groups.

Table 6. Generalized King Model Fit Parameters

pops	q	r_c	α
BS	1.80 ± 0.27	4.39 ± 0.48	-4.39 ± 0.27
RHB	0.97 ± 0.10	7.41 ± 0.93	-1.92 ± 0.33
all X-ray with bkd corr	1.51 ± 0.12	4.99 ± 0.37	-3.54 ± 0.37
qLMXBs	1.68 ± 0.31	4.62 ± 0.65	-4.03 ± 0.92
non-qLMXBs	1.40 ± 0.10	5.33 ± 0.32	-3.20 ± 0.31
CVs	1.57 ± 0.48	4.85 ± 1.07	-3.71 ± 1.50
Bright X-ray (>40 cnts)	1.82 ± 0.34	4.35 ± 0.55	-4.45 ± 1.00
Faint X-ray	1.31 ± 0.11	5.59 ± 0.39	-2.94 ± 0.33

Note. — Best-fit generalized King Model parameters for several different populations. Errors are derived from bootstrap statistics.

Table 7. Approximate Collision Parameters for a Sample of Clusters

Cluster	Γ		Sources Detected		Background	References
(1)	(2)	(3)	(4)	(5)	(6)	(7)
NGC 6266	516	500	51	...	2-3	
47 Tuc	235	434	45	79	~ 16	Heinke et al. (2005)
NGC 6626	148	186	26	...	2-3	
NGC 6093	109	166	17	19	1-2	Heinke et al. (2003)
NGC 5904	40	69	16	...	4-7	
ω Cen	23	49	28	60	19-24	Haggard et al. (2009)
NGC 6752	81	38	11	...	2-3	
NGC 7099	23	18	7	11	1-2	Lugger et al. (2007)
NGC 6121	8	13	6	6	1-3	Bassa et al. (2004)
NGC 6397	12	5.9	12	11	0-1	Bogdanov et al. (2010)
NGC 6366	2.1	2.3	4	5	2-4	Bassa et al. (2008)
NGC 6388	515	61	1-2	

Note. — Col. (2): The approximate values of Γ are shown against col. (3): the value of Γ reported by Pooley et al. (2003). Col. (4): Numbers of detected sources as reported by Pooley et al. (2003) are compared to col. (5): updated values from the literature for a limit of $4 \times 10^{30} \text{erg s}^{-1}$. The limit for NGC 6388 is $\sim 5 \times 10^{30} \text{erg s}^{-1}$. Col. (6): predicted background counts. Col. (7): sources for the updated results in col. (5).

